Asymmetrical Dependence of {Ba^{2+}}:{SO$_4^{2-}$} on BaSO$_4$ Crystal Nucleation and Growth in Aqueous Solutions: A Dynamic Light Scattering Study

Sergěj Y. M. H. Seepma,* Bonny W. M. Kuipers, and Mariette Wolthers

Read Online

ACCESS | 📊 Metrics & More | 📖 Article Recommendations | 🔗 Supporting Information

ABSTRACT: The impact of solution stoichiometry, upon formation of BaSO$_4$ crystals in 0.02 M NaCl suspensions, on the development of particle size was investigated using dynamic light scattering (DLS). Measurements were performed on a set of suspensions prepared with predefined initial supersaturation, based on the quotient of the constituent ion activity product {Ba^{2+}}-{SO$_4^{2-}$} over the solubility product K_{sp} (Ω_{barite} = {Ba^{2+}}{SO$_4^{2-}$}/K_{sp} = 100, 500, or 1000−11,000 in steps of 1000), and ion activity solution stoichiometries (r_{aq} = {Ba^{2+}}:{SO$_4^{2-}$} = 0.01, 0.1, 1, 10 and 100), at circumneutral pH of 5.5−6.0, and ambient temperature and pressure. DLS showed that for batch experiments, crystal formation with varying r_{aq} was best investigated at an initial Ω_{barite} of 1000 and using the forward detection angle. At this Ω_{barite} and set of r_{aq}, the average apparent hydrodynamic particle size of the largest population present in all suspensions increased from ~200 to ~700 nm within 10−15 min and was independently confirmed by transmission electron microscopy (TEM) imaging. Additional DLS measurements conducted at the same conditions in flow confirmed that the BaSO$_4$ formation kinetics were very fast for our specifically chosen conditions. The DLS flow measurements, monitoring the first minute of BaSO$_4$ formation, showed strong signs of aggregation of prenucleation clusters forming particles with a size in the range of 200−300 nm for every r_{aq}. The estimated initial bulk growth rates from batch DLS results show that BaSO$_4$ crystals formed fastest at near-stoichiometric conditions and more slowly at nonstoichiometric conditions. Moreover, at extreme SO$_4$-limiting conditions, barite formation was slower compared to Ba-limiting conditions. Our results show that DLS can be used to investigate nucleation and growth at carefully selected experimental and analytical conditions. The combined DLS and TEM results imply that BaSO$_4$ formation is influenced by solution stoichiometry and may aid to optimize antiscalant efficiency and regulate BaSO$_4$ (scale) formation processes.
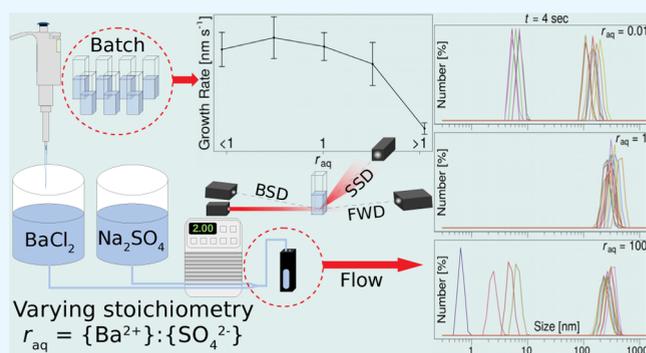
1. INTRODUCTION

Although industrial crystallization of barite (BaSO$_4$) is useful for practices such as purification and separation of solids, it is a major problem in oil and gas recovery[1−3] and in the geothermal energy industry.[4−6] Undesirable crystallization, known as "scale formation", is the formation of insoluble scale types onto surfaces of distribution piping and water handling equipment, such as pumps, valves, and heat transfer equipment. Additionally, scale formation adversely impacts the flow assurance[7−11] and the permeability of oil and gas reservoir rocks.[12−14] Barite scale is considered to be particularly difficult to deal with due to its low solubility, compared to the SrSO$_4$ and CaSO$_4$ counterparts,[15] its hardness once formed,[13] and the fact that it contributes to about 80% of the total amount of scale deposit,[16] ultimately leading to high treatment or repair costs.[17] Barite scale formation is often the result of mixing incompatible waters.[13,18−20] For example, sulfate-rich seawater is often injected into offshore reservoirs for pressure maintenance,[21,22] where it meets connate water, which often contains a high

amount of barium,[23] leading to barite formation upon mixing. Barite also occurs in limestone and sandstone deposits among others. Besides its natural occurrence and important role in oil and gas industry, barite is widely known for its inertness, high specific gravity, opaqueness to X-rays, and whiteness.[24−26] Due to these properties, barite plays a key role in the use of fillers for plastics, paint and rubber industries, and pharmaceuticals.

Ample scientific research has been dedicated to investigate the nucleation and growth of barite on both the fundamental level and from the industrial perspective. On a fundamental level, the nucleation of barite has been investigated in terms of nucleation time under varying conditions in batch experiments.[27−31] This

Table 1. Chemical Properties of the Investigated Growth Solutions[a]

solution no.	BaCl$_2$	Na$_2$SO$_4$	NaCl	calculated parameters (MINTEQ)										measured parameters		type of experiment
				{Ba^{2+}}	{SO$_4^{2-}$}	{BaCl$^+$}	{NaSO$_4^-$}	pH$_{ini}$	pH$_{eq}$	I_{ini}	I_{eq}	Ω_{barite}	r_{aq}	pH$_{ini}$	{Ba^{2+}}$_{ini}$	
1.1	1.890	1.890	9.420	1.010	0.974	0.00990	0.0605	7.096	7.079	0.0200	0.0132	10990	1.034	6.73	1.371	Batch (FWD, BSD, SSD)
1.2	1.800	1.800	10.00	0.962	0.929	0.00973	0.0594	7.095	7.079	0.0201	0.0136	10000	1.035	7.27	1.285	Batch (FWD, BSD, SSD)
1.3	1.710	1.710	10.88	0.913	0.880	0.00970	0.0592	7.094	7.079	0.0205	0.0143	8995	1.037	5.91	1.243	Batch (FWD, BSD, SSD)
1.4	1.600	1.600	11.10	0.861	0.830	0.00916	0.0559	7.093	7.079	0.0201	0.0143	7998	1.037	5.65	1.071	Batch (FWD, BSD, SSD)
1.5	1.500	1.500	12.10	0.806	0.776	0.00904	0.0551	7.092	7.079	0.0205	0.0151	6998	1.039	5.90	0.943	Batch (FWD, BSD, SSD)
1.6	1.380	1.380	12.54	0.746	0.718	0.00849	0.0517	7.091	7.079	0.0203	0.0153	5997	1.040	5.58	0.943	Batch (FWD, BSD, SSD)
1.7	1.260	1.260	13.48	0.682	0.655	0.00811	0.0493	7.090	7.079	0.0206	0.0160	5000	1.041	5.92	0.814	Batch (FWD, BSD, SSD)
1.8	1.115	1.115	13.77	0.610	0.586	0.00726	0.0442	7.089	7.079	0.0200	0.0160	3999	1.042	6.03	0.686	Batch (FWD, BSD, SSD)
1.9	0.9600	0.9600	14.58	0.529	0.507	0.00649	0.0394	7.087	7.079	0.0200	0.0165	2999	1.043	5.92	0.600	Batch (FWD, BSD, SSD)
1.10	0.7830	0.7830	15.93	0.433	0.414	0.00562	0.0341	7.086	7.079	0.0203	0.0174	2000	1.045	6.34	0.386	Batch (FWD, BSD, SSD)
1.11	0.5480	0.5408	17.10	0.306	0.292	0.00414	0.0251	7.083	7.079	0.0201	0.0181	1000	1.047	5.85	0.291	Batch (FWD, BSD, SSD)
1.12	0.3850	0.3850	17.98	0.216	0.206	0.00315	0.0182	7.084	7.078	0.0201	0.0187	500	1.049	6.25	0.180	Batch (BSD)
1.13	0.1710	0.1710	19.16	0.0970	0.0923	0.00141	0.00849	7.080	7.078	0.0200	0.0194	100	1.051	5.60	0.103	Batch (BSD)
2.1	0.05980	5.980	3.000	0.0274	3.27	0.0000634	0.228	7.132	7.132	0.0205	0.0203	1002	0.008	6.73	n.d.	Batch (FWD), Flow (BSD), TEM
2.2	0.1790	1.790	14.44	0.0920	0.970	0.00105	0.0854	7.096	7.094	0.0201	0.0194	998	0.095	5.94	n.d.	Batch (FWD), Flow (BSD), TEM
2.3	0.5480	0.5480	17.10	0.306	0.292	0.00414	0.0251	7.083	7.079	0.0201	0.0181	1000	1.047	5.85	0.291	Batch (FWD), Flow (BSD), TEM
2.4	1.790	0.1790	14.40	0.971	0.0921	0.0102	0.00639	7.080	7.078	0.0200	0.0194	1000	10.55	5.86	0.643	Batch (FWD), Flow (BSD), TEM
2.5	5.900	0.05900	2.800	3.35	0.0267	0.0365	0.000367	7.079	7.078	0.0205	0.0203	1002	125.6	5.72	2.871	Batch (FWD), Flow (BSD), TEM

[a]Concentration units are displayed in mmol L^{-1}. Forward scattering detection (FWD), backscattering detection (BSD), and side scattering detection (SSD) indicate, respectively, the forward, backscatter, and side scatter measurement detection angle; n.d. stands for not determined.

has led to several proposed empirical relationships that include various physicochemical parameters, such as temperature, supersaturation degree, geometric shape factors that describe the barite crystal, the molar volume of barite in the solution, and the (average) diffusion coefficient (which is directly related to the average particle size). The growth of barite has been investigated extensively by measuring the advance of the nanometer-sized steps at barite surfaces in contact with supersaturated aqueous solutions (*e.g.*, Putnis & Ruiz-Agudo[32]), mostly on cleaved (001) and (210) facies using atomic force microscopy (AFM)[33−40] or interferometry.[41,42] However, natural barite crystals are characterized by a wide variety of bulk morphologies. Causative is the solution's composition.[43−47] Therefore, natural barite crystals often exhibit other faces than just the cleavable (001) and (210) ones[41,48−50] (see also Widanagamage et al.[51] and references cited therein), leading to a high degree of variation in kinetics and mechanisms of barite formation and dissolution[41,52,53] and, in particular, variable rates with reaction time.[41]

On an industrial level, much of the research on barite has been focused initially on mechanical scale removal[16,18,54,55] and the application of chemical removal techniques in the oil and gas industry[56,57] (also Kamal et al.[58] and references cited therein). From these studies, it has been widely recognized that in many cases, antiscalent chemicals are the most effective and reliable way to prevent and control barite scaling problems by means of inhibition of nucleation and/or growth. For example, some antiscalent chemicals cause barite crystals with a well-faceted {001} surface to be replaced by barite crystals in which growth rates in all directions will be inhibited, leading to a loss of anisotropic growth as well as a smaller particle size.[59] Common chemicals that have been used as additives for the inhibition of barite are phosphonates and compounds with polyphosphino-carboxylic functional groups[60−68] as they are stable over a wide range of temperatures and pH, inhibit scale at low concentrations, target many types of scale, and their concentration is easily determined by colorimetric techniques.[69] However, most studies investigated the bulk phase, such as *in situ* jar tests, and research focusing on the surface chemistry in industrial settings has only taken place recently.[70−75] The main goal of those studies was to relate surface chemistry processes to the interaction behavior of barite crystals with distribution piping material and drilling fluids under specified physicochemical conditions.

While, in both settings, some research has focused on the effect of stoichiometry (which is defined as the ionic activity ratio of the constituent cation over the anion; r_{aq} = {Ba^{2+}}:{SO$_4^{2-}$}) on bulk processes, like crystal growth rates[76−79] or induction times,[80] little attention has been given to the effect of r_{aq} on the new formation (nucleation plus growth) of barite crystals. Moreover, the new formation of barite with varying r_{aq} has not been monitored extensively using dynamic light scattering (DLS). Seepma et al.[81] showed, with the use of DLS, that the {Ca^{2+}}:{CO$_3^{2-}$} affects the size and timing of new formation of CaCO$_3$ crystals. The aim of this work is to determine if r_{aq} also affects the new formation of barite crystals. Therefore, in this paper, we report particle size evolution of scaling barite in equilibrium and nonequilibrium (nucleation and growth) conditions using dynamic light scattering (DLS), and the particle size was confirmed independently by transmission electron microscopy (TEM) imaging.

2. MATERIALS AND METHODS

2.1. Growth Solutions. Visual MINTEQ—a free equilibrium speciation model—version 3.1[82] was used to define a set of growth solutions with target initial supersaturation with respect to barite (Ω_{barite}), (non-)stoichiometry between the activities of the constituent ions in barite (r_{aq}), pH, and ionic strength (I), where Ω_{barite} is defined as

$$\Omega_{barite} = \frac{\{Ba^{2+}\}\{SO_4^{2-}\}}{K_{sp}} \tag{1}$$

with K_{sp} as the solubility product of barite ($10^{-9.99}$ at 25 °C[83−85]). Different stock solutions of BaCl$_2$, Na$_2$SO$_4$, and NaCl (Merck; 99.5, 99.0, and 99.5% purity, respectively) with different concentrations were prepared, by dissolving reagent grade salts into Milli-Q water (ISO 3696 Standard Grade 1−18 mΩ), to create all of the growth solutions. Growth solutions of 50 mL were prepared from the stock solutions and kept in centrifuge tubes (Greiner), with a minimum amount of headspace, and were used to perform batch DLS experiments within 48 h. The solution's I was adjusted by the addition of NaCl (Sigma-Aldrich).

The desired growth solutions' I for these experiments was 0.02 M, which was high enough to ensure that I remained approximately constant during precipitation. The Davies equation[86] (valid for $I \leq 0.5$ M) was used to calculate {Ba^{2+}}, {SO$_4^{2-}$}, {NaSO$_4^-$}, {BaCl$^+$}. All calculations within Visual MINTEQ were done using a temperature of 20 °C, the average temperature during the experiments, and assuming a closed atmosphere. Table 1 lists all of the used growth solutions with their physicochemical parameter values.

The {Ba^{2+}} was measured using a half-cell Ba-ion-selective electrode (ISE; Mettler Toledo; serial no. DX337) in combination with a standard double-junction Ag/AgCl reference electrode (ThermoFisher Scientific; cat. no. 900200) connected to a multimeter (ThermoFisher Scientific, Orion Versa Star Pro; cat. no. VSTAR90). The Ba-ISE was calibrated with a set of standard BaCl$_2$ solutions that contained concentrations of respectively 10, 100, and 1000 ppm Ba^{2+}. The precision of the Ba-ISE was ±2−3% precision.[87] The Ba-ISE measurements were performed to confirm if the initial experimental {Ba^{2+}} was roughly in agreement with the calculated {Ba^{2+}}. Since other cations in solution interfere with the measurement (*i.e.*, potential trace Sr^{2+} ions in the 99.5%-pure BaCl$_2$ salt and Na$^+$ ions from the background electrolyte), the low accuracy of the multimeter specific to this type of measurement and the fact that our measurements were across several orders of magnitude, the inaccuracy may have been as large as 30% on top of the 2−3% precision. Note that {Ba^{2+}} was not measured for solution numbers 2.1 and 2.2 because the activity of Na$^+$ was much higher compared to Ba^{2+} and would therefore lead to a much larger inaccuracy than the aforementioned 30%. In addition to the Ba-ISE measurements, the initial pH was measured with a pH electrode (WTW; serial no. Sensolyt 900-P; precision 0.5%), connected to a multimeter (WTW; Portable pH meter Multiline 3630 IDS). Although we kept the headspace to a minimum in the solutions, respectively before and after mixing, the headspace was larger in the cuvettes that were used for DLS measurements; The maximum allowable solution in the cuvettes was 1.5 mL, meaning 2.5 mL of headspace. Therefore, it must be noted that the desired pH of the final growth solutions for each solution number (*i.e.*, 1.1− 1.13) was 7, but most likely due to quick CO$_2$ dissolution at

circumneutral conditions in very dilute systems,[88] the pH dropped quickly to ca. 5.5−6.0 right after mixing of the two growth solutions (and is more closely to the value we measured right after mixing) and continued to drop more gradually to 5.1−5.2 in the cuvette during the DLS measurement.

2.2. Dynamic Light Scattering theory. If the particles of interest can be considered to be spherical and the diameter of those particles is much smaller than the wavelength of the laser in the medium ($d_p < \lambda_{l,medium}$), then the scattering intensity (*i.e.*, irradiance) of one particle is related to the sixth power of the diameter of the particle according to the Rayleigh equation[89,90]

$$I_R = I_0 \frac{1 + \cos^2 \theta}{2s^2} \left(\frac{2\pi}{\lambda_{l,medium}} \right)^4 \left(\frac{n^2 - 1}{n^2 + 2} \right)^2 \left(\frac{d_p}{2} \right)^6 \tag{2}$$

where I_R is the (isotropic) Rayleigh scattering intensity [W m^{-2}], I_0 is the intensity of the laser beam arriving at the measured sample volume [W m^{-2}], s is the distance between the particle and the detector [m], θ is the angle between the incident beam toward the sample and the scattered beam going to the detector [°], n is the relative refractive index between the particle of interest and the chosen dispersant [−], and d_p is the particle diameter [m]. A value of 1.64 for the refractive index (n) was used for our barite in water systems. To include also particles with a size in the order of the used wavelength in the analysis, the Mie theory is used, to account for the anisotropic scattering of larger particles (Supporting Information (SI)-I). This theory includes internal reflection, refraction, and absorption, giving a scattering-angle-dependent form factor.[91,92] We used an absorption coefficient value of 0.01 cm^{-1} (*i.e.*, $4\pi k n/\lambda_{l,medium}$; with k as the extinction coefficient[93]) for all DLS experiments.

Additionally, the hydrodynamic radius R_h, where $R_h \propto d_p$, is related to the translational diffusion coefficient by the Einstein−Stokes relationship[94,95]

$$D_{Trans} = \frac{k_B T}{6 \mu \pi R_h} \tag{3}$$

where k_B is the Boltzmann constant [m^2 kg s^{-2} K^{-1}], T is the absolute temperature [K], μ is the dynamic viscosity [kg s^{-1} m^{-1}] (*i.e.*, for dilute aqueous solutions at 20 °C: 0.001 kg s^{-1} m^{-1}), and D_{Trans} is the translational diffusion coefficient [m^2 s^{-1}]. The DLS technique was used to extract D_{Trans} distribution from the autocorrelation function, which was obtained by averaging a series of intensity signals. Accordingly, the particle size intensity distribution (eq 3) was obtained and finally the (relative) number size distribution, using the Mie theory to account for the intensity weight factor (*i.e.*, to convert the intensity to number concentration).

2.3. DLS Measurement Settings and Specifications. The nucleation and growth of BaSO$_4$ were investigated using DLS with the Zetasizer ULTRA, equipped with ZS XPLORER v1.2.0.91 software.[96,97] The laser used was a red Ne-He laser with a wavelength of 632.8 nm with a power of 10 mW and a parallel beam area of 1256.6 μm^2, resulting from a laser beam diameter of 40 μm. By the time the laser arrives at the sample, the laser power has diminished somewhat and is estimated at 8 mW (S. Remijn, personal communication, April 7, 2020). Therefore, the incoming irradiance (I_0) is 0.00637 mW/μm^2. The distance s between the particle and the detector is approximately 15 mm. The initialization period of the Zetasizer ULTRA lasted from a minimum of 40 to a maximum of 60 s. All DLS measurements

were conducted at a temperature of 20 ± 0.1 °C for a set of growth solutions (Table 1).

The particle size results were obtained using the non-negative least squares as the discrete inversion approach,[98] together with the Multiple Narrow Modes approach as the regularization method, as there is a high potential for different populations during the processes of crystal nucleation and growth. Consequently, quadratic data weighing was used to amplify subtle changes in the larger and more significant correlation coefficients over noise in the baseline, and the regularizer was fixed to 0.001 and 70 fixed values for size classes were used.[99] The measurement process for the batch experiments was chosen manually and included 20 subruns that each lasted for 1.68 s (where the subrun time is defined as τ) with no pause in between for all conducted size measurements. This choice was made based on a compromise between obtaining accurate statistics and a reasonable amount of time-resolved measurements. For the flow DLS experiments, 30 subruns were chosen instead, as the time within the process of nucleation and growth was fixed; *i.e.*, measurements were performed at a specific point along the flow path, at a fixed distance after the growth solutions were brought together in a y-connector, and the solutions flowed at a constant rate. Further chosen settings during size measurements, in both batch and flow, included the automatic determination of the attenuation and the optimal measurement position within the cuvette. The optimum position was always found to be in the middle of the cuvette (*i.e.*, at 4.64 mm). Equilibration time with regards to temperature was set to 10 s, as we measured close to room temperature and aimed for the quickest way possible to start the DLS measurements after mixing the growth solutions. The error of the measured (apparent) particle size and the real particle size in the cuvette may be as large as 10% for a particle size of ±1000 nm following from Berne & Pecora[100] and Frisken.[101]

2.4. DLS Batch Measurements. The majority of the batch experiments with varying Ω_{barite} (*i.e.*, solution number 1.1−1.11) were performed in the forward scattering detection (FWD) angle at a detection angle of 12.78°, the backscattering detection (BSD) angle at a detection angle of 174.7° and the side scattering detection (SSD) angle at a detection angle of 90°. This way, we could determine which (of the) angle(s) was/were most suitable for our type of suspensions. In addition, the solutions 1.1−1.13 were measured to determine the best concentration/supersaturation range for DLS experiments on BaSO$_4$ particle size evolution, where the reaction kinetics were appropriate. Solutions 1.12 and 1.13 were only measured in FWD, due to the relatively low supersaturation compared to 1.1−1.11. Smaller particles are more accurately measured in BSD. Generally, the BSD has the advantage that the multiple scattering effect is reduced. For our type of samples, this was most relevant in the more concentrated/supersaturated solutions of 1.1−1.11[102,103] and would therefore give a more accurate measurement for the smaller-sized particles. Nevertheless, we performed FWD as well because it was very likely that in these samples a larger number of larger-sized particles would be present on a faster timescale in batch DLS measurements. The experiments at $\Omega_{barite} \geq 1000$ (*i.e.*, solution nos. 1.1−1.11 in Table 1) were run for 1500 s, while at $\Omega_{barite} < 1000$ (*i.e.*, solution nos. 1.12 and 1.13 in Table 1) were conducted for 7500 s. Furthermore, we conducted a series of batch experiments in FWD at $\Omega_{barite} = 1000$ with $r_{aq} \sim 0.01, 0.1, 1, 10,$ and 100 (solution nos. 2.1−2.5 in Table 1) to investigate the effect of stoichiometry on BaSO$_4$ formation. These series of batch DLS
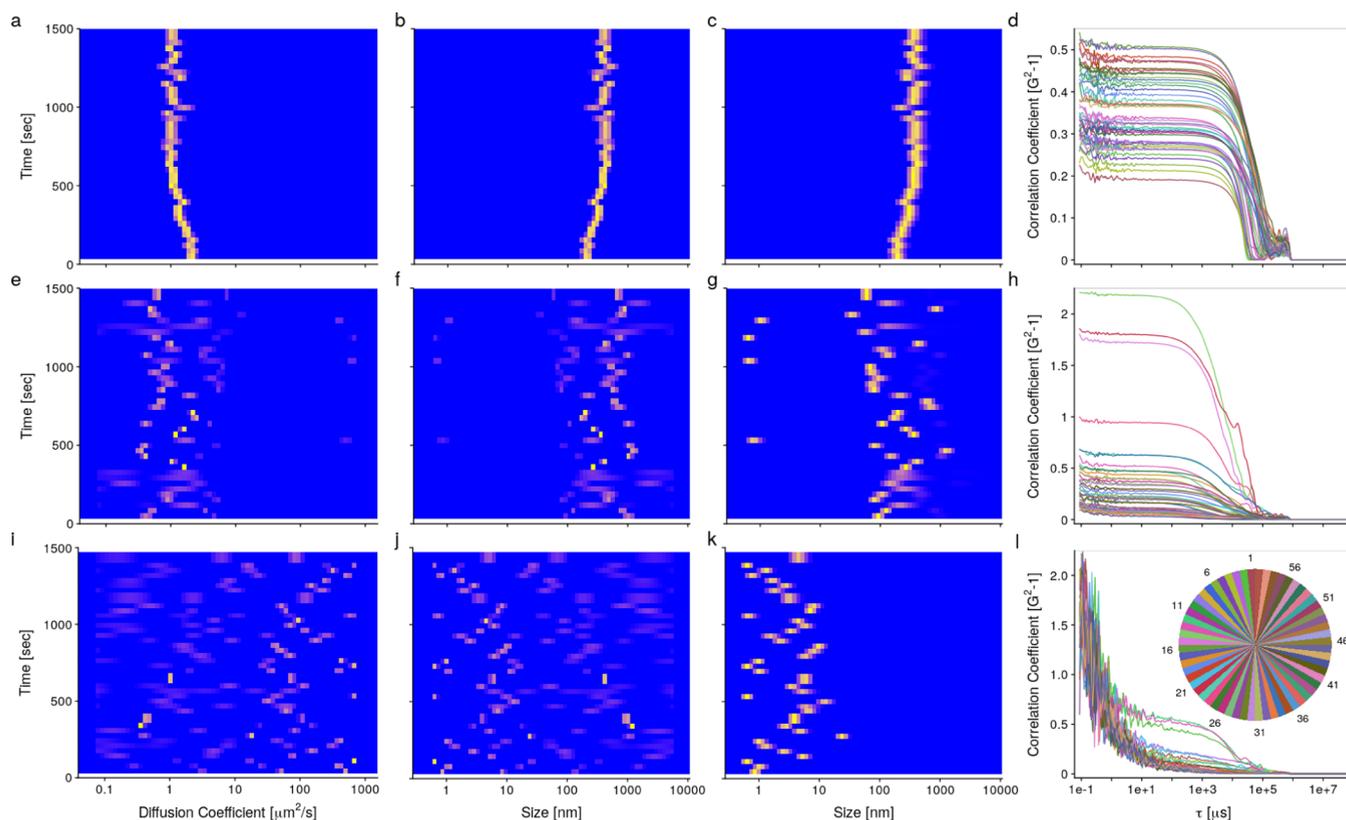
Figure 1. Diffusion coefficient distribution with time (a), intensity size distribution with time (b), (relative) number size distribution with time (c), and associated autocorrelation functions for each timestep (d) measured in the FWD at $\Omega_{barite} = 1000$. Diffusion coefficient distribution for the (e−h) BSD and (i−l) SSD.

measurements were performed over a timescale of approximately 3 h. Note that, for a complete picture, it was necessary to look at the autocorrelation functions, the diffusion coefficient distribution (derived from the autocorrelation function and (shape) model-independent), the intensity size distribution (model-dependent; assumes spherical particles), and the (relative) number size distribution (model-dependent).[104]

All of the batch experiments were taken within standard (10 × 10 mm) disposable polystyrene cuvettes, which were cleansed beforehand with Milli-Q water. Both the barium-containing and sulfate-containing solutions were squeezed through 0.2 μm disposable nylon syringe filters beforehand, to remove as much dust particles as possible. Thereafter, the solutions were mixed and poured into the cuvette, which was quickly closed and inserted in the Zetasizer ULTRA.

2.5. DLS Flow Measurements. DLS flow experiments were conducted with solution nos. 2.1, 2.3, and 2.5. The BSD angle was chosen because the measurements were done within the first minute after mixing of both growth solutions and we expected to observe mainly smaller-sized particles. The DLS flow experiments were performed using a ZEN0023 quartz glass flow-through cuvette[96] with a fitting FEP tubing set (Hellma; serial no. 040-001-722) for respectively the inflow and outflow to and from the cell. The FEP tubing was connected to Tygon tubing LMT-55, with an inner diameter of 1.52 mm (Ismatec; serial no. SC0041) and several pieces of that (extension) tubing was cut to certain lengths in such a way that the time between the point of mixing of the two growth solutions and the point that the mixed solution reached the flow cell was 4, 10, 30 or 60 s. For flow purposes, a peristaltic pump (Ismatec; serial no. IPC-N-08)

equipped with Click-n-go POM-C cassettes in combination with Tygon Long Flex tubing (two-stop-coded tubing; Ismatec serial no. SC0424), with an inner diameter of 1.52 mm and a wall thickness of 0.86 mm, was used. The different tubing was connected with nylon Y-connectors and straight connectors. To minimize the potential pressure differences between the cassettes, they were placed directly next to each other. Each measurement for a certain sample at a specific time was repeated for at least 10 times and up to 25 times. A constant flow rate of 8 mL/min was used for each of the flow DLS experiments.

For cleaning purposes between each flow experiment, 0.5 M ethylenediamine tetraacetic acid (EDTA) was pumped through the system with 8 mL/min for about 1 h. The pH of the EDTA was increased to ~8 to attain maximum chelating capacity.[105] To chelate 1 ppm of Ba^{2+}, 2.1 ppm of EDTA was necessary.[106] Since the molecular weight of EDTA is 292.24 g mol^{-1}, 0.5 M equates to a chelating capacity of 146,120 ppm. The highest barium concentration we used in our flow experiments contained 124 ppm. Therefore, the cleaning procedure was more than efficient to remove any precipitated barite in the tubing and/or cell. After the EDTA cleaning step, we pumped Milli-Q water for 30 min with 8 mL/min through the system, before a new flow experiment was started.

In DLS flow experiments, measurements were repeated at exactly the same time t and are easily compared. The differences at which the apparent particle size distribution appeared across the multiple repeat measurements (i.e., the consistency and reproducibility of the mean apparent particle size and its distribution), we referred to as the variability. This should not be confused with polydispersity, which is the distribution in one

measurement (*i.e.*, the broadness of the peak in one measurement, or the simultaneous occurrence of multiple peaks).

2.6. Determination of Growth Rates Based on DLS Data. The initial bulk crystal growth rates for solution nos. 2.1–2.5 (Table 1) were determined by linear fitting of the initial 10–15 min of the measurement. For these linear fits, the first 15 measurements were taken into account for the initial rate analysis, with the condition that the multiple R^2 was at least 40% (0.40). This value represents a moderately good value for the variance of simple linear models explaining stochastic processes like crystal formation and, thus, was considered statistically valid.[107] For this reason, some data points were excluded at r_{aq} = 100 (the excluded points are red in Figure 3) and were replaced by the nearest data points so that the 15 data points closest to t = 0 s formed a linear regression with a multiple $R^2 > 0.40$.

2.7. TEM Imaging. TEM imaging was conducted on solids sampled from solution nos. 2.1–2.5 after 2 and 5 min from the moment when the two growth solutions were mixed. From each growth solution, 1 mL was pipetted into a cuvette, mixed, and after the selected time, 50 μL of the suspension was drop-cast on a standard copper grid (200 mesh). The copper grids contained a 28–30 nm layer of carbon film and were made hydrophilic by glow discharge prior to drop-casting. The liquid in the pipetted volume was absorbed by the filter paper beneath the copper grid; the particles in the suspension remained on the grid and were dry after ±3 min. The imaging was performed at 200 keV on the Tecnai20 of the university's Electron Microscopy Centre.

3. RESULTS AND DISCUSSION

Batch DLS experiments were conducted for a set of solutions, where the initial Ω_{barite} varied from 1000 to 11,000 with steps of 1000 plus 100 and 500, all at r_{aq} = 1 (stoichiometric conditions), pH ∼ 5.5–6.0, I ∼ 0.02 M and NaCl as the background electrolyte (BE), to investigate which initial Ω_{barite} and what scattering angles were useful to measure our type of (developmental) suspensions. In short, the results for solution nos. 1.1–1.13 (SI-II) indicate that batch nucleation and growth measurements on BaSO$_4$ aqueous solutions could best be conducted at Ω_{barite} ∼ 1000 because enough particles were formed in solution (*i.e.*, the signal-to-noise ratio was as good as it could be for our type of evolving suspensions) and the reaction kinetics were slow enough to monitor the (expected) particle size change. In addition, the forward detection angle showed the most distinct increase in apparent particle size over time. In the following subsection, details are provided per measurement angle (Section 3.1).

3.1. Angular Scattering Effect on DLS Measurement Results. Figure 1 shows the DLS results for the experiment at Ω_{barite} = 1000 at stoichiometric conditions for the different measurement angles. The circle diagram (as inset in Figure 1l) shows the pallet of colors that correspond to the colors that have been used for the autocorrelation functions (*i.e.*, Figure 1d,h,l) so that their chronological order within the experiment is portrayed. The results for all of the initial Ω_{barite} values are found in SI-II, as well as details on the data treatment.

3.1.1. Forward Scattering Detection (FWD) Angle. The FWD results showed consistent autocorrelation functions (Figure 1d), with a cutoff value (*y*-axis) between 0.2 and 0.5, which is lower than the ideal cutoff values (contrast) of 0.8–1.0. However, this was expected considering the stochastic nature of the systems we measured. In addition, the last part of those autocorrelation functions showed sinusoidal behavior, which might be related to a certain degree of sedimentation of the

larger-sized particles in the system (see SI-III and SI-IV for discussion on sedimentation). In FWD, we observed one dominant apparent particle size at around 200 nm that became larger with time. Since only one dominant population was observed in FWD, the intensity size distribution (Figure 1b) was very similar to the (relative) number size distribution (Figure 1c) and the diffusion coefficient distribution (Figure 1a) showed the opposite trend because larger particles diffuse more slowly in solution than smaller particles (eq 3).

3.1.2. Backscattering Detection (BSD) Angle. The signal in the BSD was dominated by smaller-sized particles, including those that surpassed their critical size (SI-V) and the larger-sized particles measured in FWD were underrepresented. Therefore, the BSD signal may have been more sensitive to the (stochastic) nucleation processes that form the smaller particles. Indeed, the BSD showed slightly less consistent autocorrelation functions (Figure 1h) compared to the FWD (Figure 1d). Most of the BSD autocorrelation functions yielded (relative) number size distributions between roughly 20 and 2000 nm. However, some yielded bimodal particle size intensity distributions around 1 and 100–200 nm (Figure 1f). Note that the autocorrelation functions for these bimodal particle size distributions showed cutoff values above 1.0. For static, stable suspensions, the cutoff value cannot exceed 1.0 because that would mean that there was more overlap (correlation) between the initial intensity signal (*i.e.*, t = 0; t_0) and $t_0 + \tau$, as time progressed. Contrastingly, the intensity signals from our evolving suspensions may show increased correlation after some time due to the (stochastic) evolution of the suspension. In the current case, a bimodal size distribution was observed, with prenucleation clusters (*i.e.*, smaller than the calculated critical size of 5.5 nm; SI-V), alongside the larger-sized particles (Figure 1g).

3.1.3. Side Scattering Detection (SSD) Angle. The SSD results showed a multimodal and stochastic picture of the diffusion coefficient distributions (Figure 1i) and intensity particle size distributions (Figure 1j), which showed multiple populations for each measurement in the experiment. Due to the sixth-order dependence of the scattering intensity on particle size (eq 2), the smallest-sized particles dominated the resulting relative number particle size distribution (Figure 1k). Generally, particles <10 nm were observed throughout the measurements. However, in all cases, the autocorrelation functions had cutoff values > 1.0 (Figure 1l) and the SSD autocorrelation functions also lacked the typical decay-curve shape. This implies that the measurement volume in the SSD was too low, due to the angle between the laser beam and the detector (0.1 nL), to be used properly in the systems that we investigated, resulting in a low signal-to-noise ratio. Therefore, it is likely that an insufficient amount of particles scatter toward the SSD and that the correlation functions were dominated by noise. This conjecture is supported by the fact that the larger particles (>100 nm in apparent size) were hardly visible in SSD, while in the BSD measurements, where, generally speaking, larger particles are more difficult to detect, the larger particles were still detected. Therefore, the SSD results were ignored in the remainder of this study.

3.2. BaSO$_4$ Crystal Nucleation in DLS Flow Experiments. The BSD flow experiments capture the initial particle formation processes that take place at t < 1 min in contrast to the batch experiments, which had a lower time resolution. These measurements were performed in BSD because we expected smaller-sized particles shortly after mixing the two growth solutions. Figure 2e–h shows the relative number particle size
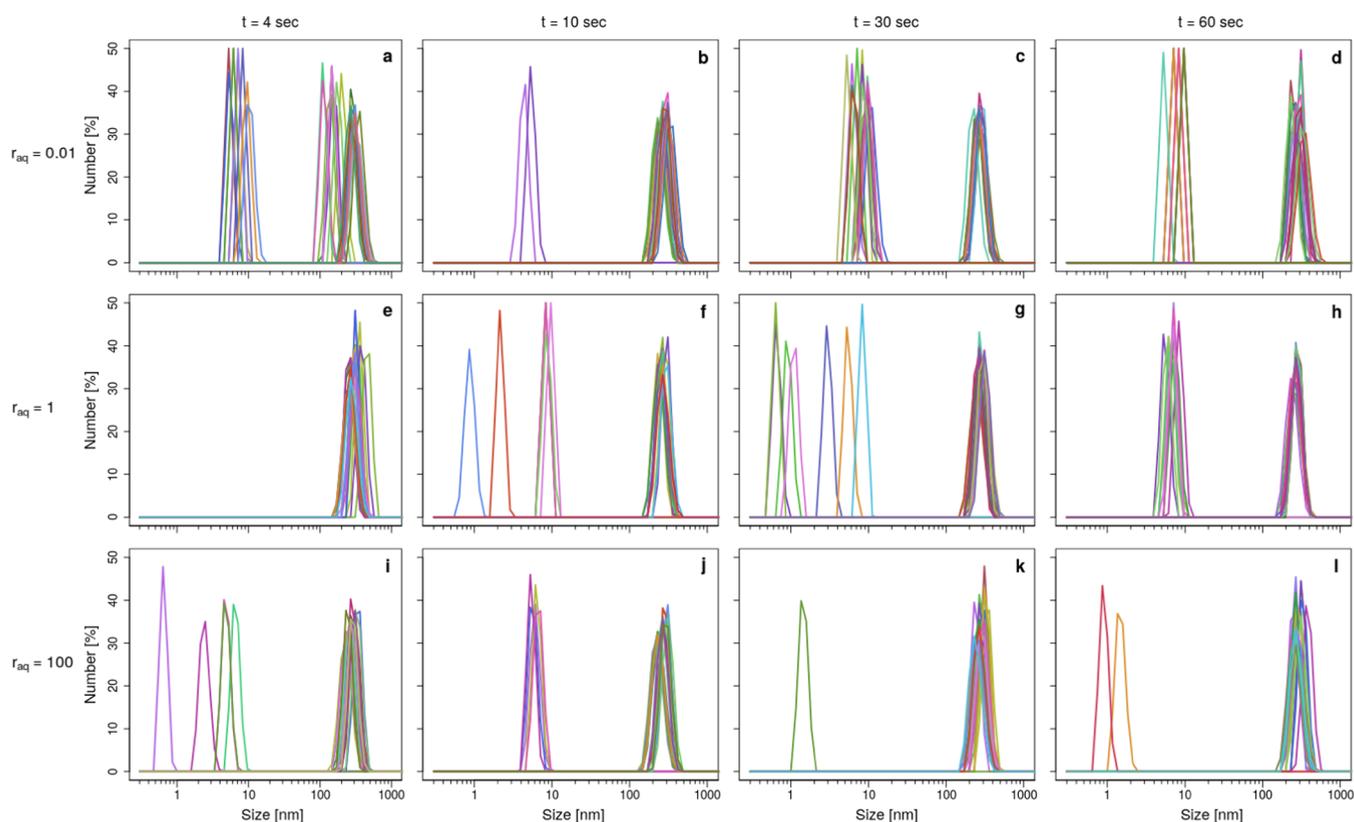
Figure 2. Particle size number distributions for r_{aq} = 0.01, 1, and 100 at Ω_{barite} = 1000 at specific time steps (4, 10, 30, and 60 s) after the onset of the barite precipitation reaction. More specifically, the particle size number distributions are shown for r_{aq} = 0.01 at t = 4 s (a), t = 10 s (b), t = 30 s (c), and t = 60 s (d); for r_{aq} = 1 at t = 4 s (e), t = 10 s (f), t = 30 s (g), and t = 60 s (h); and for r_{aq} = 100 at t = 4 s (i), t = 10 s (j), t = 30 s (k), and t = 60 s (l).

information at t = 4, 10, 30, and 60 s for r_{aq} = 1 after mixing the growth solutions. The associated autocorrelation functions, diffusion coefficient distributions, and the intensity particle size distributions are found in Figures S20e–h, S21e–h, and S22e–h in SI–V, respectively.

The dominant apparent particle size at r_{aq} = 1 for Ω_{barite} = 1000 was in the order of 200 to 300 nm, which matched the apparent particle size observed at the first timestep in the batch experiment of Figure 1c (the same initial conditions). Particles with sizes of 200–300 nm were observed within 4 s after mixing. This suggests that under these physicochemical conditions, BaSO$_4$ crystal nucleation occurred nearly instantaneously. This is in agreement with Söhnel & Mullin,[28] who found that the induction time (defined as the first moment at which a particle reaches its critical size[108]) is <1 s for BaSO$_4$ under our physicochemical conditions and, thus forms its crystalline structure rapidly.[109] In addition, the variability in the apparent particle sizes of 200 to 300 nm became slightly less over time where, at t = 60 s (Figure 2h), the peaks were well aligned at an apparent particle size of 300 nm. This would mean that some more crystal growth already occurred on the particles that were initially 200 nm in size.

Besides the dominant larger-sized particles, we also observed peaks at the size range of 1 to 20 nm, with a larger degree of stochasticity. These peaks were significantly more present at t = 10, 30, and 60 s than in the batch BSD experiment (*i.e.*, Figure 2f–h versus Figure 1g). Remarkably, the particles of 1 to 20 nm in size were not present at t = 4 s at r_{aq} = 1 (also not in the duplicate; Figure S23e). This may be explained by the high degree of rapid aggregation of prenucleation clusters (Section 3.4), at conditions where the Ω_{barite} was still close to the initial

supersaturation (Ω_{barite} = 1000), 4 s after mixing the barium and sulfate solutions. As a result, prenucleation clusters were formed more abundantly and more quickly since Ba^{2+} ions had a larger probability to meet SO$_4^{2-}$ ions and vice versa. The prenucleation clusters that were observed at t = 10 s (Figure 2f) were more frequently observed at t = 30 s (Figure 2g) and became less variable in apparent size at t = 60 s (Figure 2h). In addition, the apparent size of the smallest prenucleation clusters (*i.e.*, 1–5 nm) at t = 10 and 30 s disappeared in favor of particle sizes of approximately 7 nm at t = 60 s after mixing. This observation may be related to the fact that Ω_{barite} decreased along the flow path due to barite formation, and that growth of the prenucleation clusters started to be more favored over the aggregation of those same clusters for t > 4 s.

Extrapolating these results to the batch results under the same initial conditions (Figure 1g), where the first measurement was completed within t = 90–120 s after mixing, the number of prenucleation clusters became significantly less compared to the nucleated and growing particles. Most likely, these prenucleation clusters got incorporated in the larger crystals, which explains why we observed a slight growth of the larger-sized particles already, during the first minute after initiation of the BaSO$_4$ batch precipitation reaction.

3.3. Effect of Stoichiometry on BaSO$_4$ Crystal Nucleation. Besides DLS flow experiments at r_{aq} = 1, we also performed flow DLS experiments at Ω_{barite} = 1000 and r_{aq} = 0.01 and 100, to investigate the effect of stoichiometry (r_{aq}) on BaSO$_4$ crystal nucleation. Figure 2a–d,i–l shows the relative number particle size information at t = 4, 10, 30, and 60 s after mixing of the growth solutions for, respectively, r_{aq} = 0.01 and 100. In addition, the autocorrelation functions, diffusion coefficient
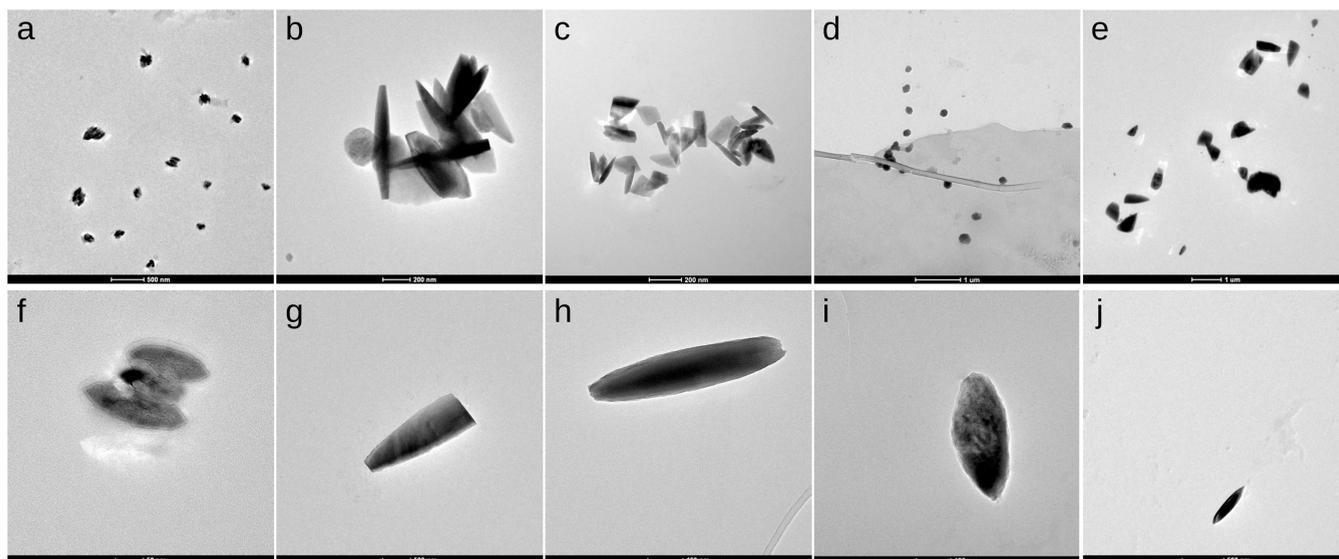
Figure 3. TEM images of the formed $BaSO_4$ crystals after 2 min of reaction for r_{aq} = 0.01 (a, f), 0.1 (b, g), 1 (c, h), 10 (d, i), 100 (e, j). A more general overview of the sample is shown in the top row (a−e), while the single particle morphology is shown in the bottom row (f−j). Note that the crystal orientation for f−j varies.

distributions, and the intensity particle size distributions are found in Figures S20a−d, S21a−d, S22a−d and S20i−l, S21i−l and S22i−l in SI−VI, respectively, for r_{aq} = 0.01 and 100.

The most striking effect of stoichiometry was observed in the results at t = 4 s after mixing (Figure 2a,e,i). While smaller-sized particles were not observed for r_{aq} = 1 (Figure S21e), they were observed at nonstoichiometric conditions, resulting in bimodal size distributions for $r_{aq} \neq 1$. At sulfate-excess conditions (r_{aq} = 0.01), the smaller-sized population fluctuated between 5−20 nm and the larger-sized populations fluctuated between 100−400 nm (Figure 2a). At barium-excess conditions (r_{aq} = 100), the smaller particles remained <10 nm and the larger particles in the order of 300 nm (Figure 2i). Although we cannot quantify the difference in nucleation rates, this difference suggests slower nucleation rates at nonstoichiometric conditions, with less favorable nucleation conditions at Ba excess than at SO_4 excess.

With increasing time after mixing of the growth solutions, continued appearance of peaks in the apparent size range of 1−20 nm suggests that these smaller (prenucleation) clusters coexisted with larger (nucleated and growing) particles. The apparent size of the prenucleation clusters at r_{aq} = 100 was consistently somewhat smaller at t = 4, 30, and 60 s than those at r_{aq} = 0.01, which may indicate that nucleation was somewhat slower at r_{aq} = 100 compared to r_{aq} = 0.01.

3.4. TEM Imaging. Figure 3 shows the morphology of the formed $BaSO_4$ crystals representative of those observed in FWD after 2 min of reaction time for r_{aq} = 0.01, 0.1, 1, 10, and 100. Figure 3a−e illustrates a more general overview of the sample, while Figure 3f−j represents the morphology in terms of a single particle or aggregate. The morphology after 5 min of reaction time for different conditions of r_{aq} is found in SI−VII. In line with Bracco et al.,[78] we found that our $BaSO_4$ particles for r_{aq} > 1 were generally more rounded compared to $r_{aq} \leq 1$, where the rounding of particles at r_{aq} = 100, became prominent after 5 min (SI−VII). It is likely, that the rounding for r_{aq} = 100 was delayed, relative to r_{aq} = 10, due to slower growth (Section 3.5). Noticeable was that at r_{aq} = 0.01, we formed small aggregates after 2 min (Figure 3a,f), likely the result of oriented aggregation of nuclei that were 2−10 nm in size.[110] For r_{aq} = 0.1 and 1,

we observed that the formed crystals started twinning on some occasions (Figure 3b,c), but were coexistent with single crystals (Figure 3g,h and SI−VII). After 5 min, twinned crystals were relatively less common for r_{aq} < 1 compared to $r_{aq} \geq 1$ (SI−VII). Based on our TEM results, we can conclude that, depending on r_{aq}, the DLS results represented predominantly single particles or small oriented aggregates.

Figure 3c,h shows that the $BaSO_4$ particles were in the order of 200 nm after 2 min along the *ab*-direction of the crystals (lateral size). Due to our ionic strength conditions, the double-layer thickness ranged between 2.1 and 2.3 nm among different r_{aq} conditions as well as from initial to equilibrium conditions and, therefore, we assumed $d_h \sim d_p$. Hence, the particle size we observed in TEM matched with our initial particle size in the corresponding DLS batch experiment (Figure 4c), as well as with the reproducible peak observed at 200−300 nm in our DLS flow measurements for r_{aq} = 1 (Figure 2e−h). For r_{aq} = 0.01, based on Figure 5a,f, we can conclude that the lateral particle size of a single aggregate coincides with our particle size observations in the corresponding DLS batch (Figure 4a) and flow (Figure 2a−d) experiments. However, for r_{aq} = 0.1, we observed a larger particle size in the TEM observations (Figure 3b,g) compared to the initial batch DLS measurements (Figure 4b) (*i.e.*, with the equal circle area assumption, we estimated that the lateral particle size of a single particle in TEM was about 360−380 nm). The more common occurrence of twinning crystals at r_{aq} = 0.1 (Figure 3b) may have contributed to a relatively larger variability in particle size early on in the DLS batch experiment (Figure 4b) compared to other r_{aq} conditions. For r_{aq} = 10 and 100, the particle size in TEM (Figure 3d,i and e,j respectively) roughly matched those in our initial batch DLS experiments (Figure 4d,e), although the particles for r_{aq} = 100 show a large degree of variability in particle size in TEM (Figure 4e). Despite that the particle size for r_{aq} = 0.1 was found to be (significantly) larger than in DLS, our TEM work shows that we formed $BaSO_4$ crystals during DLS experiments and their particle sizes generally matched well.

3.5. Effect of Stoichiometry on $BaSO_4$ Crystal Growth. Figure 4 shows time-resolved batch measurements (2−3 h) of
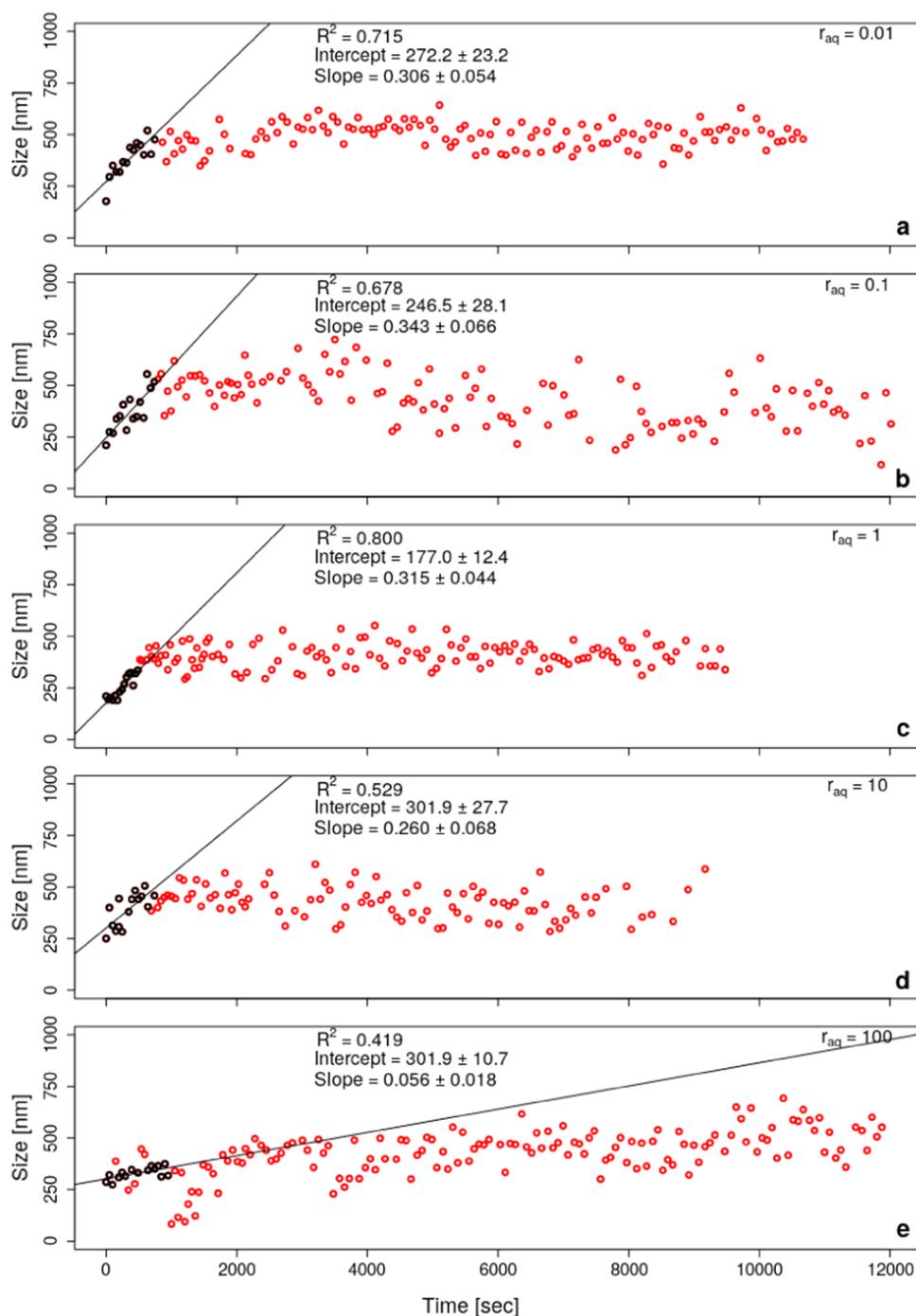
Figure 4. BaSO$_4$ particle size evolution as a function of time for r_{aq} = 0.01 (a), 0.1 (b), 1 (c), 10 (d), and 100 (e) at Ω_{barite} = 1000 in FWD. The initial bulk crystal growth rates were determined with linear regression for the first 15 data points that fulfilled the requirement $R^2 \geq 0.40$. Therefore, some data points were left out (in red) and the nearest other data points were taken into account (in black) for r_{aq} = 100.

the apparent particle size for a series of batch solutions, with varying r_{aq}, 0.01, 0.1, 1, 10, 100, at pH ~ 5.5−6.0, I ~ 0.02 M, Ω_{barite} = 1000 and NaCl as BE in FWD. Figure 4a−e shows the weighted average of the relative number particle size distribution on a linear scale. The predominant particle size (*i.e.*, the hydrodynamic diameter) observed for the different r_{aq} conditions was always between 100 and 700 nm. In addition, the apparent size increased within the first half an hour at every r_{aq} from 200−300 nm to about 600−700 nm. Only at r_{aq} = 100, the apparent particle size increase was not so rapid initially, but more gradual throughout the experiment. Also, at r_{aq} = 100, a

rapid increase in size was reproducibly observed at 1500−2000 s and at about ~4000 s. This could be associated with multiple nucleation events occurring at those time steps. Alternatively, it could be an oscillatory particle size behavior, which may originate from the dissolution of a precursor phase and subsequent new formation of a more stable barite phase. This conjecture in impurity-free systems was only recently suggested by Ruiz-Agudo et al.,[111] based on TEM and titration experiments. Although their TEM images could also be interpreted as primary, disorderly aggregated (nanocrystalline) subunits (*e.g.*, Wolthers et al.[112] and Brunner & Cölfen[113]), their
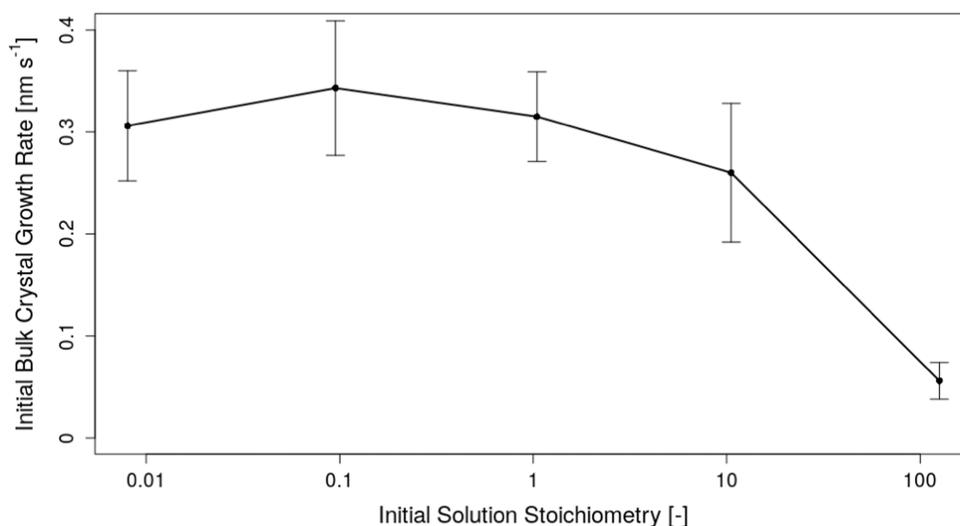
Figure 5. Initial bulk crystal formation rate [nm/s] versus initial solution stoichiometry [−] at initial Ω_{barite} = 1000, pH ~ 7.1 (Table 1) in 0.02 M NaCl solutions. The relation shows an asymmetrical dependence. The uncertainty is portrayed with error bars.

TEM images clearly show a transition from aggregates, consisting of ca. 5−10 nm-sized subunits, to a clearly crystalline euhedral phase. In our experiments, it is quite likely a similar transition occurred, although our data cannot confirm or rule out if this is *via* dissolution of the aggregates or *via* a different transformation process.

The initial increase in apparent particle size (Figure 4) was assumed to represent the initial bulk crystal growth rate. The number particle size distributions for the data points that were used are shown in Figure S25 (SI−VIII). Although this way of analysis may be challenging due to the stochasticity of particle formation (see SI−VIII for the discussion), we can conclude that crystal growth was fastest (steepest slope) at r_{aq} = 0.1 with an initial bulk crystal growth rate of 0.343 nm/s (based on diameter, thus volume). The initial bulk crystal growth rate at the ideal r_{aq} = 1 is not far from this fastest rate (0.315 nm/s). Limited values are found in the literature for comparison because most bulk crystal growth studies are based on conductivity or turbidity measurements, which result in values with units of M/min or equivalent to that. In addition, AFM work reports crystal growth rates only for specific directions (*i.e.*, usually the dominant [100] and [120] directions). However, we found one study by Matynia et al.,[114] which reported a $BaSO_4$ initial bulk crystal growth rate of 0.652 nm/s for their experiment that matched best with our chosen conditions (*i.e.*, stoichiometric conditions, natural pH, unseeded), but was performed at lower ionic strength, at 315 K rather than our 293 K and $(NH_4)_2SO_4$ was used instead of Na_2SO_4. Nonetheless, their value is in the same order of magnitude as our reported value.

At larger sulfate excess, the initial bulk crystal growth rate decreased slightly to 0.306 nm/s. At barium excess, the crystal growth rates decreased to 0.26 nm/s for r_{aq} = 10 and 0.06 nm/s for r_{aq} = 100 (Figure 4). Figure 4 shows that the initial crystal growth rate is not symmetrically dependent on stoichiometry and tends to decrease much faster when SO_4^{2-} is limiting compared to Ba^{2+}-limiting solutions. A critical note should be made with respect to the results at r_{aq} = 100 because the size increase that occurred at t = 1000−2000 s could also represent the actual crystal growth, if the particles that formed first are a precursor phase like that proposed by Ruiz-Agudo[111] since the

crystal nucleation time may have been delayed significantly due to moderate nonstoichiometric conditions. In this case, when taking the first 15 points from where the apparent particle size increases rapidly at ~t = 1000, the slope would equate to a value of 0.294 nm/s, which is slightly larger than at r_{aq} = 10 and closer to the range of the values obtained at other r_{aq}. Therefore, it cannot be ruled out which of the two represents crystal growth more accurately. Still, at r_{aq} = 100 in both flow and batch BSD experiments, barite nucleation was observed to occur within the first 4 s (Figures 2 and S21−S23). Therefore, we assume the initial rate reflects the crystal growth rate and that was indeed significantly lower at r_{aq} = 100 (0.06 nm/s versus 0.343 nm/s). Despite that Figure 5 shows generally that the initial crystal growth rate decreases with more extreme values of r_{aq}, we want to point out that the standard deviations on the rates for each r_{aq} are relatively large and most of the trend is within error. For example, the difference between the initial crystal growth rate at r_{aq} = 0.01 and 1 is statistically not significant. However, the difference between r_{aq} = 1 and r_{aq} = 10 is statistically relevant and certainly between stoichiometric conditions and r_{aq} = 100. Also, R^2 is largest for r_{aq} = 1 (*i.e.*, 0.8) and drops off slightly toward r_{aq} < 1 (~0.7), meaning that the stochasticity of initial crystal growth was larger at r_{aq} < 1 compared to stoichiometric conditions. At r_{aq} > 1, R^2 was significantly lower (0.4−0.5) and therefore proceeded more stochastically compared to r_{aq} ≤ 1.

Important to note is that, with DLS measurements, we cannot distinguish between different crystal growth mechanisms. For example, our $BaSO_4$ crystals may have grown as a result of a spiral growth mechanism, that proceeds under surface-controlled conditions, where new edges were continuously generated, due to the development of screw dislocations.[115] This type of crystal growth has been widely observed in kinetic studies involved with $BaSO_4$[34,40,116−121] especially at Ω_{barite} < 80.[40] This type of crystal growth may have occurred in our systems when the solution was slowly approaching equilibrium conditions. Yet, crystals may also have grown by aggregation of prenucleation clusters, in particular early on in the experiments, since at Ω_{barite} > 80 the spiral growth mechanism is not expectedly dominant. Ruiz-Agudo et al.[122] found, based on TEM work, that two hierarchical levels of aggregation during $BaSO_4$ formation could occur, where particles with a size range

of 5−10 nm form larger nanometer-sized (20−60 nm) particles and subsequently aggregate into larger-sized crystals of 200−500 nm. They used experimental conditions relatively similar to ours, but with a slightly larger supersaturation (*i.e.*, $\Omega_{barite} \sim 5000$ and $r_{aq} = 1$). Although these authors used ethanol to quench the barite crystallization process before TEM imaging, which may have affected the $BaSO_4$ crystals in a different way compared to our samples, a similar process of aggregation of prenucleation clusters could have occurred in our system as well. In particular, the flow DLS measurements showed strong signs of (multiple stages of) aggregation behavior, where consistent and reproducible peaks at 10−20 and at 200−300 nm were observed (Figure 2). Also, the observation that intermediate-sized particles (20−200 nm) are generally absent in our experiments at all detection angles (Figures 1c,g,k, and 2), would coincide with such aggregation behavior. We have not found any signs of two-dimensional (2D)-nucleation on our barite crystals (Figure 3). This is consistent with existing work, which only showed signs of 2D nucleation on barite crystals in the [001] direction at $\Omega_{barite} > 1000$.[33,34,36,40]

3.6. Asymmetrical Dependence of Crystal New Formation on Solution Stoichiometry. Barite new formation was observed here to be faster, resulting in larger (prenucleation) clusters being observed earlier at ideal and barium-limited conditions (Figures 2 and 4). A similar nonsymmetrical dependence of crystal new formation on solution stoichiometry was previously reported by Seepma et al.[81] for $CaCO_3$. For both $BaSO_4$ and $CaCO_3$, the combined process of nucleation and growth is greatly hindered at nonstoichiometric conditions compared to pure crystal growth of these minerals under ideal 1:1 conditions,[76,77,79,123−125] but in our case more by the lack of anions than cations. Perhaps this may be explained by a ligand-exchange-like process, where cations are generally considered to take up the central position in aqueous complexes, coordinated to several (anion) ligands.[126−128] The cations in the process of nucleation may also sit central in the (prenucleation) clusters that form, collecting one or more anions around them. This would mean that such (prenucleation) clusters can have more anions than cations and a slight limitation in cations is not critically limiting to particle nucleation (and subsequent growth). To the authors' knowledge, it is uncommon for (simple inorganic) anions to coordinate to multiple cations in aqueous complexes because anions are generally much larger than cations and, therefore, require a considerably greater size of cationic ligands.[129] Therefore, we propose it is less likely that prenucleation clusters with high cation/anion ratios are formed, and therefore the process of particle formation is hindered more severely when the cation/anion ratio increases beyond the ideal stoichiometric value. The flow DLS measurements at $t = 4$ s may indicate a similar trend, where more and slightly larger (~ 10 nm) particles appeared at Ba-limiting conditions than at SO_4-limiting conditions, where infrequently <10 nm-sized particles were observed (Figure 2a versus i and S22a versus S22i in SI−VI). Kang et al.[79] found an opposite trend (*i.e.*, crystal growth is more hindered by the lack of cations than anions) using the ZN98 creation-propagation-collision (CPC) type model[130] to model the *in situ* AFM data of Kowacz et al.[77] However, the experiments of Kowacz et al.[77] were performed near equilibrium, where they used $\Omega_{barite} \leq 12.6$ in their experiments. Our asymmetric behavior coincides more with the results of Kucher et al.,[76] who performed their experiments also far from

equilibrium (*i.e.*, their Ω_{barite} range in their experiments was 62,500−1,000,000).

Alternatively, variations in sodium and chloride concentrations with r_{aq} may have led to asymmetry in the nucleation dependency on r_{aq}. The difference in total Na or Cl concentration at extreme r_{aq} compared to $r_{aq} = 1$ is at most 83% (*i.e.*, 83% difference in the total Na concentrations in solution no. 2.3 compared to 2.5). However, the NaCl concentration in all of these solutions is in the regime where the mobility of the lattice ions is affected by the ion charge distribution, rather than a change in the bulk solvent structure by NaCl, which occurs at larger concentrations.[131] For higher-ionic-strength conditions than ours (0.03 versus 0.02 M) and at stoichiometric conditions, Kowacz et al.,[131] showed that $\sim 99.97\%$ of the Ba^{2+} is consumed during $BaSO_4$ formation, meaning that NaCl is negligibly incorporated in the crystal lattice. Additionally, MINTEQ calculations indicate that only minor fractions of Ba and SO_4 ions are forming ion pairs with the monovalent ions (Table 1). Though we cannot exclude any distinct impact of the monovalent ions on nanoparticle formation or aggregation, it is nevertheless unlikely that Na and Cl contribute (strongly) to the asymmetric dependency of barite nucleation r_{aq} via incorporation into the nuclei or ion pairing.

To summarize, our findings clearly show that the formation (nucleation plus growth) of barite varies with $\{Ba^{2+}\}:\{SO_4^{2-}\}$. Formation rate, particle size evolution, crystal morphologies, and twinning behavior are affected by solution stoichiometry at the conditions for our experiments. These findings can be considered as a first step in unraveling the impact of solution stoichiometry on the combined processes of barite nucleation and growth and more detailed work is needed to further unravel the potentially different nucleation and growth pathways. The observation of distinct particle size evolution and occurrence of rounded surfaces at different moments in the formation process (Figures 3 versus S24) hints at potentially different sensitivity of barite forming at nonstoichiometric conditions toward surfactants and antiscaling agents.

3.7. Limitations in DLS Experiments. In the model to process raw DLS data to hydrodynamic radii and particle sizes, an important but invalid assumption is that the particles are spherical (see our TEM results, Figure 3 and SI−VII). In addition, numerous studies have shown that different morphologies exist, depending on the physicochemical conditions of the solution from which barite precipitated (*e.g.*, Dunn et al.,[44] Voigt & Sundmacher[132] and Godinho & Stack[41]), where morphology varied from bladed-shaped crystals to dendritic-shaped crystals. In most of these previously reported cases as well as for our TEM-observed crystals, the *c*-directions grew more slowly than the *a*- and *b*-directions of the crystals. Furthermore, it is expected that similar shapes occurred in the experiments for which we have not shown TEM data. Moreover, due to gravity, the crystals may have had a preferred orientation in our cuvettes during the DLS experiments. This was not accounted for. On top of that, crystals nucleated and grew under constantly changing conditions within one experiment because Ω_{barite} dropped, to a lesser extent I dropped and, at extreme r_{aq}, r_{aq} shifted toward more extreme values by several magnitudes as well. This was previously discussed for similar experiments with $CaCO_3$ by Seepma et al.[81] These changing conditions likely have caused more heterogeneity with regard to crystal formation rates and morphology over time during batch DLS experiments and were also not accounted for.

Second, the Tygon tubing used in the flow experiments is thought to limit any buildup of virtually all inorganic compounds, due to the smoothened and polished inner wall (Saint-Gobain Performance Plastics, 2019). Yet, we cannot rule out that heterogeneous nucleation on the tubing may have played a significant role in the flow DLS experiments as numerous studies have shown that polymers can act as a substrate (*i.e.*, Vekilov[133] and references cited therein). Consequently, Ω_{barite} may have dropped more or differently in the sample at a certain time after mixing compared to that same time in batch cuvette DLS experiments, due to the different setup (*i.e.*, Section 2.4 versus Section 2.5). However, note that in our DLS measurements, no stagnant heterogeneously nucleated particles on cuvette and tubing wall can be observed, since they do not show Brownian motion. Moreover, our DLS results show that, if this effect played a role, it did not significantly impact the apparent particle size distribution because we observed, for example, similar apparent particle sizes in the first measurement of the batch DLS experiment at $r_{aq} = 1$ (*i.e.*, roughly at 60 s) (Figure 4c) and at that same condition and time for the flow DLS measurements (Figure 2h).

Third, some degree of sedimentation of the largest particles in our systems toward equilibrium has occurred during the batch DLS experiments. This was observed most prominently in the autocorrelation functions for the FWD after ∼30 min (Figure 1d) (see also discussion in SI-III and SI-IV, where we showed that gravitational settling of particles may contribute more to the apparent (measured) diffusion coefficient (and thus the particle size), compared to the contribution of Brownian motion, at particles sizes > 700 nm). Subsequently, sedimentation may have caused a generally larger variability in the weighted average particle sizes toward the end of the experiments (near equilibrium conditions), compared to the beginning of each batch DLS experiment (Figure 4), as less particles likely end up in the measurement volume and, thus, stochasticity increased.

Finally, the challenge of investigating barite formation is the very low solubility ($K_{sp} = 10^{-9.99}$), which meant we had to work with a high degree of supersaturation to create enough material that lead to an appropriate signal-to-noise ratio. We propose that the initially used Ω_{barite} value of 1000 leads to an intermediate particle concentration that provided sufficient signal while minimizing aggregation.

3.8. Implications. Our research has shown that DLS is a suitable technique to investigate nucleation and growth of BaSO$_4$ (barite), although the low solubility product combined with the necessity to produce sufficiently high numbers of scattering particles leads to a narrow range of conditions where the reaction mechanism and kinetics can be investigated. More generally, our work implies that DLS is applicable to investigate the formation of inorganic crystals, especially for systems with a somewhat higher solubility product. It must be noted that, at higher particle densities, different settings of the Zetasizer may be necessary, such as the detection angle and the number of subruns for a right balance between statistics and the number of time-resolved measurements.

Considering barite new formation, we have shown that solution stoichiometry impacts the nucleation and growth asymmetrically at $\Omega_{barite} = 1000$. Most likely, a similar trend can be observed at other Ω_{barite} conditions far from equilibrium and, consequently, it is important to know the solution barium-to-sulfate ratio to predict barite formation rates in natural and engineered settings. Moreover, guiding a solution stoichiometry is a way to tailor barite formation (rate), even without the need

for inhibitors, to improve processes that take place in the petroleum, chemical, paint, and filler industries.[119,134−136] Potentially, solution stoichiometry (at a constant degree of barite supersaturation) may enhance or reduce the effect additives have on barite (scale) formation. For example, Kowacz et al.[77] showed that barite precipitation rates could be increased in 5 vol % methanol or move toward $r_{aq} \sim 5$ for systems at low and constant supersaturation (*i.e.*, $\Omega_{barite} = 12.6$). But even without additive, our results show that altering the solution barium-to-sulfate ratio affects the barite crystallization rate and, ultimately, controls the timescale and amount of barite deposition.

4. CONCLUSIONS

Our experimental results show that the $\{Ba^{2+}\}{:}\{SO_4^{2-}\}$ in the solution during barite nucleation and growth has a strong and asymmetrical impact on the particle size development of the newly formed barite particles. Our results show that DLS can be used to investigate nucleation and growth at carefully selected experimental and analytical conditions. At a constant initial degree of supersaturation ($\Omega_{barite} = 1000$), BaSO$_4$ crystals

- grow from about 200 nm to approximately 700 nm within 15−30 min
- may have formed by aggregation of prenucleation clusters (<10 nm) toward a size of 200−300 nm
- grow faster at near-stoichiometric and barium-limiting conditions than at sulfate-limiting conditions
- vary in aggregation and twinning behavior with solution stoichiometry

These observations imply that the efficiency of antiscalants, which often target barite growth-specific crystallographic orientations, may depend on solution $\{Ba^{2+}\}\{SO_4^{2-}\}$. Therefore, ultimately, solution stoichiometry may be used in tailoring natural and engineered BaSO$_4$ crystallization processes.

■ ASSOCIATED CONTENT

ⓢ **Supporting Information**

The Supporting Information is available free of charge at https://pubs.acs.org/doi/10.1021/acsomega.2c07418.

> Details on Mie theory (I), motivation for chosen DLS settings (II), calculations regarding sedimentation influence in DLS (III + IV), critical nucleus size calculations (V), additional data on DLS flow experiments (VI), supporting TEM images (VII), and number particle size distributions associated with Figure 4 (VIII) (PDF)

■ AUTHOR INFORMATION

Corresponding Author

> **Sergĕj Y. M. H. Seepma** − *Department of Earth Sciences, Utrecht University, 3584 CB Utrecht, The Netherlands;* ⓞ orcid.org/0000-0002-9033-8528;
> Email: s.y.m.h.seepma@uu.nl

Authors

> **Bonny W. M. Kuipers** − *Van 't Hoff Laboratory for Physical and Colloid Chemistry, Debye Institute for Nanomaterials Science, Utrecht University, 3584 CH Utrecht, The Netherlands*
> **Mariette Wolthers** − *Department of Earth Sciences, Utrecht University, 3584 CB Utrecht, The Netherlands;* ⓞ orcid.org/ 0000-0003-3908-5622

■ REFERENCES

(1) Benton, W. J.; Collins, I. R.; Grimsey, I. M.; Parkinson, G. M.; Rodger, S. A. Nucleation, growth and inhibition of barium sulfate-controlled modification with organic and inorganic additives. *Faraday Discuss.* **1993**, *95*, 281−297.

(2) Bahadori, A.; Zahedi, G.; Zendehboudi, S. Estimation of potential barium sulfate (barite) precipitation in oilfield brines using a simple predictive tool. *Environ. Prog. Sustainable Energy* **2013**, *32*, 860−865.

(3) Kamari, A.; Gharagheizi, F.; Bahadori, A.; Mohammadi, A. H. Rigorous modeling for prediction of barium sulfate (barite) deposition in oilfield brines. *Fluid Phase Equilib.* **2014**, *366*, 117−126.

(4) Scheiber, J.; Ravier, G.; Sontot, O.; Hensch, C.; Genter, A.In situ material studies at the High Temperature Skid (HTS) bypass system of the geothermal power plant in Soultz-sous-Forêts, France. In *Proceedings of the 38th Workshop on Geothermal Reservoir Engineering*; Stanford University: Stanford, CA, USA, 11−13 February, 2013; pp 1103−1111.

(5) Griffiths, L.; Heap, M. J.; Wang, F.; Daval, D.; Gilg, H. A.; Baud, P.; Schmittbuhl, J.; Genter, A. Geothermal implications for fracture-filling hydrothermal precipitation. *Geothermics* **2016**, *64*, 235−245.

(6) Tranter, M.; De Lucia, M.; Kühn, M. Numerical investigation of barite scaling kinetics in fractures. *Geothermics* **2021**, *91*, No. 102027.

(7) Vetter, O. J.; Kandarpa, V.; Harouaka, A. Prediction of scale problems due to injection of incompatible waters. *J. Pet. Technol.* **1982**, *34*, 273−284.

(8) Bezerra, M. C. M.; Khalil, C. N.; Rosario, F. F.Barium and strontium sulfate scale formation due to incompatible water in the Namorado Fields Campos Basin, Brazil. Presented at *SPE Latin America Petroleum Engineering Conference*, Rio de Janeiro, Brazil, 14-19 October, 1990. DOI: 10.2118/21109-MS.

(9) Sorbie, K. S.; Mackay, E. J. Mixing of injected, connate and aquifer brines in waterflooding and its relevance to oilfield scaling. *J. Pet. Sci. Eng.* **2000**, *27*, 85−106.

(10) Mackay, E. J.; Jordan, M. M.; Torabi, F.Predicting Brine Mixing Deep Within the Reservoir, and the Impact on Scale Control in Marginal and Deepwater Developments. Presented at the *International Symposium and Exhibition on Formation Damage Control*, Lafayette, LA, USA, 20-21 February, 2002. DOI: 10.2118/73779-MS.

(11) Zhen-Wu, B. Y.; Dideriksen, K.; Olsson, J.; Raahauge, P. J.; Stipp, S. L. S.; Oelkers, E. H. Experimental determination of barite dissolution and precipitation rates as a function of temperature and aqueous fluid composition. *Geochim. Cosmochim. Acta* **2016**, *194*, 193−210.

(12) Baraka-Lokmane, S.; Sorbie, K. S. Effect of pH and scale inhibitor concentration on phosphonate-carbonate interaction. *J. Pet. Sci. Eng.* **2010**, *70*, 10−27.

(13) Mavredaki, E.; Neville, A.; Sorbie, K. S. Initial stages of barium sulfate formation at surfaces in the presence of inhibitors. *Cryst. Growth Des.* **2011**, *11*, 4751−4758.

(14) Senthilmurugan, B.; Ghosh, B.; Sanker, S. High performance maleic acid based oil well scale inhibitors—development and comparative evaluation. *J. Ind. Eng. Chem.* **2011**, *17*, 415−420.

(15) Wu, X.Formation Damage by Inorganic Deposition. In *Formation Damage During Improved Oil Recovery: Fundamentals and Application*; Yuan, B.; Wood, D. A., Eds.; Gulf Professional Publishing: Oxford, U.K., 2018; pp 217−242.

(16) Cowan, J. C.; Weintritt, D. J.*Water-formed Scale Deposits*; Gulf Publishing Company, Book Division: TX, USA, 1976.

(17) Collins, I. R.Predicting the location of barium sulfate scale formation in production systems. Presented at *SPE International Symposium on Oilfield Scale*, Aberdeen, Scotland, 11-12 May, 2005. DOI: 10.2118/94366-MS.

(18) Frenier, W. W.; Ziauddin, M.*Formation, Removal, and Inhibition of Inorganic Scale in Oilfield Environment*; Society of Petroleum Engineers: Richardson, TX, USA, 2008.

(19) Kelland, M. A.*Production Chemicals for the Oil and Gas Industry*; CRC Press: Boca Raton, FL, USA, 2014.

(20) Movahedi, H.; Shad, S.; Mokhtari-Hosseini, Z. B. Modeling and simulation of barite deposition in an annulus space of a well using CFD. *J. Pet. Sci. Eng.* **2018**, *161*, 476−496.

(21) Moghadasi, J.; Jamialahmadi, M.; Müller-Steinhagen, H.; Sharif, A.; Ghalambor, A.; Izadpanah, M. R.; Motaie, E.Scale formation in Iranian oil reservoir and production equipment during water injection. Presented at *SPE International Symposium on Oilfield Scale*, Aberdeen, Scotland, 29-30 January, 2003. .

(22) Alotaibi, M. B.; Nasr-El-Din, H. A.Chemistry of Injection Water and Its Impact on Oil Recovery in Carbonate and Clastics Formations. Presented at *SPE International Symposium on Oilfield Chemistry*, The Woodlands, Texas, 20−22 April, 2009. .

(23) Hardy, J. A.; Simm, I. Low sulfate seawater mitigates barite scale. *Oil Gas J.* **1996**, *94*, 64−67.

(24) López-Quintela, M. A.; Rivas, J. Chemical reactions in microemulsions: a powerful method to obtain ultrafine particles. *J. Colloid Interface Sci.* **1993**, *158*, 446−451.

(25) Joselevich, E.; Willner, I. Photosensitization of quantum-size TiO_2 particles in water-in-oil microemulsions. *J. Phys. Chem. A* **1994**, *98*, 7628−7635.

(26) Hang, J. Z.; Zhang, Y. F.; Shi, L. Y.; Feng, X. Electrokinetic properties of barite nanoparticles suspensions in different electrolyte media. *J. Mater. Sci.* **2007**, *42*, 9611−9616.

(27) Wojciechowski, K.; Kibalczyc, W. Light scattering study of KH_2PO_4 and $BaSO_4$ nucleation process. *J. Cryst. Growth* **1986**, *76*, 379−382.

(28) Söhnel, O.; Mullin, J. W. Interpretation of crystallization induction periods. *J. Colloid Interface Sci.* **1988**, *123*, 43−50.

(29) Van der Leeden, M. C.; Kashchiev, D.; Van Rosmalen, G. M. Precipitation of barium sulfate: Induction time and the effect of an additive on nucleation and growth. *J. Colloid Interface Sci.* **1992**, *152*, 338−350.

(30) Tomson, M. B.; Fu, G.; Watson, M. A.; Kan, A. T. Mechanisms of Mineral Scale Inhibition. *SPE Prod. Facil.* **2003**, *18*, 192−199.

(31) Albertovna, S. L.; Sergeevich, T. D. Kinetics of Barium Sulfate Cristallisation at the Process its Spontaneous Precipitation in an aqueous Solution. *Int. J. Appl. Eng. Res.* **2016**, *11*, 7926−7928.

(32) Putnis, C. V.; Ruiz-Agudo, E. The mineral-water interface: where minerals react with the environment. *Elements* **2013**, *9*, 177−182.

(33) Bosbach, D.; Hall, C.; Putnis, A. Mineral precipitation and dissolution in aqueous solution: in-situ microscopic observations on barite (001) with atomic force microscopy. *Chem. Geol.* **1998**, *151*, 143−160.

(34) Pina, C. M.; Bosbach, D.; Prieto, M.; Putnis, A. Microtopography of the barite (001) face during growth: AFM observations and PBC theory. *J. Cryst. Growth* **1998a**, *187*, 119−125.

(35) Higgins, S. R.; Bosbach, D.; Eggleston, C. M.; Knauss, K. G. Kink dynamics and step growth on barium sulfate (001): a hydrothermal scanning probe microscopy study. *J. Phys. Chem. B* **2000**, *104*, 6978−6982.

(36) Risthaus, P.; Bosbach, D.; Becker, U.; Putnis, A. Barite scale formation and dissolution at high ionic strength studied with atomic force microscopy. *Colloids Surf., A* **2001**, *191*, 201−214.

(37) Kowacz, M.; Putnis, A. The effect of specific background electrolytes on water structure and solute hydration: Consequences for crystal dissolution and growth. *Geochim. Cosmochim. Acta* **2008**, *72*, 4476−4487.

(38) Ruiz-Agudo, E.; Putnis, C. V. Direct observations of mineral fluid reactions using atomic force microscopy: the specific example of calcite. *Mineral. Mag.* **2012**, *76*, 227−253.

(39) de Antonio Gómez, S.; Pina, C. M.; Martin-Bragado, I. Lattice kinetic modeling of the anisotropic growth of two-dimensional islands on barite (001) surface. *Cryst. Growth Des.* **2013**, *13*, 2840−2845.

(40) Kuwahara, Y.; Liu, W.; Makio, M.; Otsuka, K. In Situ AFM Study of Crystal Growth on a Barite (001) Surface in $BaSO_4$ Solutions at 30 °C. *Minerals* **2016**, *6*, 117.

(41) Godinho, J. R. A.; Stack, A. G. Growth kinetics and morphology of barite crystals derived from face-specific growth rates. *Cryst. Growth Des.* **2015**, *15*, 2064−2071.

(42) Vital, M.; Daval, D.; Morvan, G.; Martinez, D. E.; Heap, M. J. Barite Growth Rates as a Function of Crystallographic Orientation, Temperature and Solution Saturation State. *Cryst. Growth Des.* **2020**, *20*, 3663−3672.

(43) Shikazono, N. Precipitation mechanisms of barite in sulfate-sulfide deposits in back-arc basins. *Geochim. Cosmochim. Acta* **1994**, *58*, 2203−2213.

(44) Dunn, K.; Daniel, E.; Shuler, P. J.; Chen, H. J.; Tang, Y.; Yen, T. F. Mechanisms of surface precipitation and dissolution of barite: a morphology approach. *J. Colloid Interface Sci.* **1999**, *214*, 427−437.

(45) Zhang, M.; Zhang, B.; Li, X.; Yin, Z.; Guo, X. Synthesis and surface properties of submicron barium sulfate particles. *Appl. Surf. Sci.* **2011**, *258*, 24−29.

(46) Bunney, K.; Freeman, S.; Ogden, M. I.; Richmond, W. R.; Rohl, A. L.; Jones, F. Effect of lanthanum on the crystal growth of barium sulfate. *Cryst. Growth Des.* **2014**, *14*, 1650−1658.

(47) Boon, M.; Jones, F. Barium sulfate crystallization from synthetic seawater. *Cryst. Growth Des.* **2016**, *16*, 4646−4657.

(48) Goldschmidt, V.*Atlas der krystalformen (Vol. 1)*; C. Winter: Heidelberg, Germany, 1913.

(49) Piana, S.; Jones, F.; Gale, J. D. Assisted desolvation as a key kinetic step for crystal growth. *J. Am. Chem. Soc.* **2006**, *128*, 13568−13574.

(50) Stack, A. G. Molecular dynamics simulations of solvation and Kink Site formation at the {001} Barite-Water interface. *J. Phys. Chem. C* **2009**, *113*, 2104−2110.

(51) Widanagamage, I. H.; Waldron, A. R.; Glamoclija, M. Controls on barite crystal morphology during abiotic precipitation. *Minerals* **2018**, *8*, 480.

(52) Pina, C. M.; Becker, U.; Risthaus, P.; Bosbach, D.; Putnis, A. Molecular-scale mechanisms of crystal growth in barite. *Nature* **1998**, *395*, 483−486.

(53) Smith, M. E.; Knauss, K. G.; Higgins, S. R. Effects of crystal orientation on the dissolution of calcite by chemical and microscopic analysis. *Chem. Geol.* **2013**, *360−361*, 10−21.

(54) Crabtree, M.; Eslinger, D.; Fletcher, P.; Miller, M.; Johnson, A. Fighting scale: removal and prevention. *Oilfield Rev.* **1999**, *11*, 30−45.

(55) Davies, M.; Scott, P. J. B.*Oilfield Water Technology*: NACE International: Houston, TX, USA, 2006.

(56) Van Rosmalen, G. M.; Van der Leeden, M. C.; Gouman, J. The influence of inhibitors on the growth of barium sulfate crystals in suspension: Scale prevention (II). *Krist. Tech.* **1980**, *15*, 1269−1277.

(57) Benton, W. J.; Collins, I. R.; Grimsey, I. M.; Parkinson, G. M.; Rodger, S. A. Nucleation, growth and inhibition of barium sulfate-controlled modification with organic and inorganic additives. *Faraday Discuss.* **1993**, *95*, 281−297.

(58) Kamal, M. S.; Hussein, I.; Mahmoud, M.; Sultan, A. S.; Saad, M. A. Oilfield scale formation and chemical removal: A review. *J. Pet. Sci. Eng.* **2018**, *171*, 127−139.

(59) Coveney, P. V.; Davey, R.; Griffin, J. L. W.; He, Y.; Hamlin, J. D.; Stackhouse, S.; Whiting, A. A new design strategy for molecular recognition in heterogeneous systems: a universal crystal-face growth inhibitor for barium sulfate. *J. Am. Chem. Soc.* **2000**, *122*, 11557−11558.

(60) Black, S. N.; Bromley, L. A.; Cottier, D.; Davey, R. J.; Dobbs, B.; Rout, J. E. Interactions at the organic/inorganic interface: binding motifs for phosphonates at the surface of barite crystals. *J. Chem. Soc., Faraday Trans.* **1991**, *87*, 3409−3414.

(61) Davey, R. J.; Black, S. N.; Bromley, L. A.; Cottier, D.; Dobbs, B.; Rout, J. E. Molecular design based on recognition at inorganic surfaces. *Nature* **1991**, *353*, 549−550.

(62) Hen, J.; Brunger, A.; Peterson, B. K.; Yuan, M. D.; Renwick, J. P.A Novel Scale Inhibitor Chemistry for Downhole Squeeze Application in High Water Producing North Sea Wells. Presented at *SPE International Symposium on Oilfield Scale*, Aberdeen, Scotland, 5-8 September, 1995. DOI: 10.2118/30410-MS.

(63) Rohl, A. L.; Gay, D. H.; Davey, R. J.; Catlow, C. R. A. Interactions at the Organic/Inorganic Interface: Molecular Modeling of the Interaction between Diphosphonates and the Surfaces of Barite Crystals. *J. Am. Chem. Soc.* **1996**, *118*, 642−648.

(64) Lakatos, I.; Lakatos-Szabo, J.; Kosztin, B.Comparative study of different barite dissolvers: technical and economic aspects. Presented at *the International Symposium and Exhibition on Formation Damage Control*, Lafayette, LA, USA, 20-21 February, 2002. .

(65) Jones, F.; Stanley, A.; Oliveira, A.; Rohl, A. L.; Reyhani, M. M.; Parkinson, G. M.; Ogden, M. I. J. The role of phosphonate speciation on the inhibition of barium sulfate precipitation. *J. Cryst. Growth* **2003**, *249*, 584−593.

(66) Laing, N.; Graham, G. M.; Dyer, S. J.Barium Sulphate Inhibition in Subsea Systems − The Impact of Seabed Temperatures on the Performance of Generically Different Scale Inhibitor Species. Presented at *the International Symposium on Oilfield Chemistry*, Houston, Texas, 5-7 February, 2003. DOI: 10.2118/80229-MS.

(67) Pina, C. M.; Putnis, C. V.; Becker, U.; Biswas, S.; Carroll, E. C.; Bosbach, D.; Putnis, A. An atomic force microscopy and molecular simulations study of the inhibition of barite growth by phosphonates. *Surf. Sci.* **2004**, *553*, 61−74.

(68) Wang, F.; Xu, G.; Zhang, Z.; Song, S.; Dong, S. A systematic morphosynthesis of barium sulfate in the presence of phosphonate inhibitor. *J. Colloid Interface Sci.* **2006**, *293*, 394−400.

(69) Browning, F. H.; Fogler, H. S. Precipitation and dissolution of calcium-phosphonates for the enhancement of squeeze lifetimes. *SPE Prod. Facil.* **1995**, *10*, 144−150.

(70) Quddus, A.; Allam, I. M. $BaSO_4$ scale deposition on stainless steel. *Desalination* **2000**, *127*, 219−224.

(71) Graham, A. L.; Vieille, E.; Neville, A.; Boak, L. S.; Sorbie, K. S.Inhibition of BaSO4 at a Hastelloy metal surface and in solution: The consequences of falling below the Minimum Inhibitor Concentration (MIC). Presented at *SPE International Symposium on Oilfield Scale*, Aberdeen, Scotland, 26-27 May, 2004. DOI: 10.2118/87444-MS.

(72) Ruiz-Agudo, C.; Putnis, C. V.; Putnis, A. The effect of a copolymer inhibitor on baryte precipitation. *Mineral. Mag.* **2014**, *78*, 1423−1430.

(73) Nascimento, D. R.; Oliveira, B. R.; Saide, V. G. P.; Magalhães, S. C.; Scheid, C. M.; Calçada, L. A. Effects of particle-size distribution and solid additives in the apparent viscosity of drilling fluids. *J. Pet. Sci. Eng.* **2019**, *182*, No. 106275.

(74) Mohamed, A.; Elkatatny, S.; Mahmoud, M.; Shawabkeh, R.; Al-Majed, A. Evaluating the effect of using micronised barite on the properties of water-based drilling fluids. *Int. J. Oil, Gas Coal Technol.* **2020**, *25*, 1−18.

(75) Saide, V. G. d. P.; de Oliveira, B. R.; do Nascimento, C. S.; de Oliveira Borges, R. F.; Scheid, C. M.; Calçada, L. A. Influence of solids concentration and solid/polymer interaction on the apparent viscosity of drilling fluids. *Braz. J. Chem. Eng.* **2021**, *38*, 47−60.

(76) Kucher, M.; Babic, D.; Kind, M. Precipitation of barium sulfate: Experimental investigation about the influence of supersaturation and free lattice ion ratio on particle formation. *Chem. Eng. Process.* **2006**, *45*, 900−907.

(77) Kowacz, M.; Putnis, C. V.; Putnis, A. The Effect of Cation:Anion Ratio in Solution on the Mechanism of Barite Growth at Constant Supersaturation: Role of the Desolvation Process on the Growth Kinetics. *Geochim. Cosmochim. Acta* **2007**, *71*, 5168−5179.

(78) Bracco, J. N.; Gooijer, Y.; Higgens, S. R. Hydrothermal atomic force microscopy observations of barite step growth rates as a function of the aqueous barium-to-sulfate ratio. *Geochim. Cosmochim. Acta* **2016**, *183*, 1−13.

(79) Kang, J.; Bracco, J. N.; Rimstidt, J. D.; Zhu, G. H.; Huang, F.; Zhu, C. Ba attachment and detachment fluxes to and from barite surfaces in ^{137}Ba-enriched solutions with variable $[Ba^{2+}]/[SO_4^{2-}]$ ratios near solubility equilibrium. *Geochim. Cosmochim. Acta* **2022**, *317*, 180−200.

(80) He, S.; Oddo, J. E.; Tomson, M. B. The inhibition of gypsum and barite nucleation in NaCl brines at temperatures from 25 to 90 °C. *Appl. Geochem.* **1994**, *9*, 561−567.

(81) Seepma, S. Y. M. H.; Ruiz-Hernandez, S. E.; Nehrke, G.; Soetaert, K.; Philipse, A. P.; Kuipers, B. W.; Wolthers, M. Controlling CaCO$_3$ Particle Size with $\{Ca^{2+}\}:\{CO_3^{2-}\}$ Ratios in Aqueous Environments. *Cryst. Growth Des.* **2021**, *21*, 1576−1590.

(82) Gustafsson, J. P. *Visual Minteq v3.1, a Free Equilibrium Speciation Model*; KTH, Department of Land and Water Resources Engineering: Stockholm, Sweden, 2013, http://vminteq.lwr.kth.se/.

(83) Morris, R. L.; Paul, J. *Method for Removing Alkaline Sulfate Scale*. U.S. Patent US4980077, 1990.

(84) Allison, J. D.; Brown, D. S.; Novo-Gradac, K. J. *MINTEQA2/PRODEFA2, a geochemical assessment model for environmental systems: version 3.0 user's manual* Environmental Research Laboratory, Office of Research and Development, US Environmental Protection Agency, EPA/600: Athens, GA, USA; 1991.

(85) Kuwahara, Y. In Situ Atomic Force Microscopy study of dissolution of the barite (001) surface in water at 30 °C. *Geochim. Cosmochim. Acta* **2011**, *75*, 41−51.

(86) Davies, C. W. *Ion Association*; Butterworths, 1962.

(87) Mettler Toledo International Inc. *Barium Ion Selective Electrode Application Guide*, ME-30261125; Mettler Toledo International Inc., 2015.

(88) Riché, E.; Carrié, A.; Andin, N.; Mabic, S. High-purity water and pH. *Am. Lab.* **2006**, *38*, 22.

(89) Strutt, J. W. LVIII. On the scattering of light by small particles. *Lond. Edinb. Dublin Philos. Mag. J. Sci.* **1871**, *41*, 447−454.

(90) Seinfeld, J. H.; Pandis, S. N. *Dynamics of Single Aerosol Particles*. In *Atmospheric Chemistry and Physics: From Air Pollution to Climate Change*, 2nd ed.; John Wiley & Sons Inc, 2006; pp 396−433.

(91) Kerker, M. *The Scattering of Light and Other Electromagnetic Radiation*; Academic: New York, USA, 1969.

(92) Hahn, D. W. *Light Scattering Theory*; Department of Mechanical and Aerospace Engineering; University Florida: FL, USA, 2009.

(93) Dresselhaus, M. S. *Solid State Physics Part II: Optical Properties of Solids* (Lecture Notes); Massachusetts Institute of Technology Cambridge: MA, USA, 2001. web.mit.edu/course/6/6.732/www/6.732-pt2.pdf.

(94) Einstein, A. On the movement of small particles suspended in stationary liquids required by the molecular kinetic theory of heat (English translation). *Ann. Phys.* **1905**, *322*, 549−560.

(95) Sutherland, W. LXXV. A dynamical theory of diffusion for non-electrolytes and the molecular mass of albumin. *Lond. Edinb. Dublin Philos. Mag. J. Sci.* **1905**, *9*, 781−785.

(96) Malvern Panalytical Ltd. *Zetasizer Advance Series User Guide*, MAN0592-06-EN, issue 1.1; Malvern Panalytical Ltd.2020a.

(97) Malvern Panalytical Ltd. *Zetasizer Advance Series Basic Guide*, MAN0593-05-EN, issue 1.1; Malvern Panalytical Ltd.2020b.

(98) Brown, W. *Dynamic Light Scattering: The Method and Some Applications*; Oxford Clarendon Press: England, 1993.

(99) Shaw, R. *Dynamic Light Scattering Training: Achieving Reliable Nano Particle Sizing*, Malvern Instruments Ltd.2014 https://www.chem.uci.edu/~dmitryf/manuals/Fundamentals/DLS%20concept.pdf (accessed 2020-08-14).

(100) Berne, B. J.; Pecora, R. *Dynamic Light Scattering: With Applications to Chemistry, Biology, and Physics*; General Publishing Company Ltd.: Canada, 2000.

(101) Frisken, B. J. Revisiting the method of cumulants for the analysis of dynamic light-scattering data. *Appl. Opt.* **2001**, *40*, 4087−4091.

(102) Wiese, H.; Horn, D. Single-mode fibers in fiber-optic quasielastic light scattering: A study of the dynamics of concentrated latex dispersions. *J. Chem. Phys.* **1991**, *94*, 6429−6443.

(103) Peters, R.; Georgalis, Y.; Saenger, W. Accessing lysozyme nucleation with a novel dynamic light scattering detector. *Acta Crystallogr., Sect. D: Biol. Crystallogr.* **1998**, *54*, 873−877.

(104) Planken, K. L.; Kuipers, B. W. M.; Philipse, A. P. Model independent determination of colloidal silica size distributions via analytical ultracentrifugation. *Anal. Chem.* **2008**, *80*, 8871−8879.

(105) Martell, A. E.; Calvin, M. *Chemistry of the Metal Chelate Compounds*; Prentice-Hall Inc.: NY, USA, 1952.

(106) Ostroff, A. G. *Introduction to Oilfield Water Technology*, 2nd ed.; Houston, TX, USA, 1979.

(107) Frost, J. *Regression Analysis: An intuitive Guide for Using and Interpreting Linear Models*; Statistics by Jim, PA, USA, 2019.

(108) De Yoreo, J. J.; Vekilov, P. G. Principles of crystal nucleation and growth. *Rev. Mineral. Geochem.* **2003**, *54*, 57−93.

(109) Nielsen, A. E. *Kinetics of Precipitation*; Oxford Pergamon Press: U.K., 1964.

(110) Ruiz-Agudo, C.; Ruiz-Agudo, E.; Putnis, C. V.; Putnis, A. Mechanistic principles of barite formation: from nanoparticles to micron-sized crystals. *Cryst. Growth Des.* **2015**, *15*, 3724−3733.

(111) Ruiz-Agudo, C.; McDonogh, D.; Avaro, J. T.; Schupp, D. J.; Gebauer, D. Capturing an amorphous BaSO$_4$ intermediate precursor to barite. *CrystEngComm* **2020**, *22*, 1310−1313.

(112) Wolthers, M.; Van der Gaast, S. J.; Rickard, D. The structure of disordered mackinawite. *Am. Mineral.* **2003**, *88*, 2007−2015.

(113) Brunner, J.; Cölfen, H. *Progress in Mesocrystal Formation*. In *Crystallization via Nonclassical Pathways Volume 1: Nucleation, Assembly, Observation & Application*; Zhang, X., Ed.; American Chemical Society: Washington, DC, USA, 2020. DOI: 10.1021/bk-2020-1358.ch004.

(114) Matynia, A.; Piotrowski, K.; Koralewska, J.; Wierzbowska, B. Barium Sulfate Crystallization Kinetics in the Used Quenching Salts Treatment Process. *Chem. Eng. Technol.* **2004**, *27*, 559−568.

(115) Olson, I. A.; Shtukenberg, A. G.; Kahr, B.; Ward, M. D. Dislocations in molecular crystals. *Rep. Prog. Phys.* **2018**, *81*, No. 096501.

(116) Nielsen, A. E. Nucleation and Growth of Crystals at High Supersaturation. *Krist. Tech.* **1969**, *4*, 17−38.

(117) Leung, W. H.; Nancollas, G. H. Nitrilotri (methylenephosphonic acid) adsorption on barium sulfate crystals and its influence on crystal growth. *J. Cryst. Growth* **1978a**, *44*, 163−167.

(118) Leung, W. H.; Nancollas, G. H. A kinetic study of the seeded growth of barium sulfate in the presence of additives. *J. Inorg. Nucl. Chem.* **1978**, *40*, 1871−1875.

(119) Gardner, G. L.; Nancollas, G. H. Crystal growth in aqueous solution at elevated temperatures. Barium sulfate growth kinetics. *J. Phys. Chem. B* **1983**, *87*, 4699−4703.

(120) Vere, A. W. *Crystal Growth: Principles and Progress*; Plenum Press: NY, USA, 1987.

(121) Thompson, R. G. *Interactions of Polyelectrolyte Crystal-Growth Inhibitors with BaSO$_4$ Surfaces*. In *Colloid-Polymer Interactions: Particulate, Amphiphilic, and Biological Surfaces*; Dubin, P. L.; Tong, P., Eds.; Marathon Oil Company: Littleton, CO, USA, 1993; pp 182−192.

(122) Ruiz-Agudo, C.; Putnis, C. V.; Ruiz-Agudo, E.; Putnis, A. TEM analysis of the initial stages of BaSO$_4$ crystallization. In *Geophysical Research Abstracts, 2014 European Geosciences Union General Assembly (EGU 2014)* Vienna, Austria; Paper EGU2014-2939.

(123) Larsen, K.; Bechgaard, K.; Stipp, S. L. S. The effect of the Ca^{2+} to CO$_3^{2-}$ activity ratio on spiral growth at the calcite $\{10\bar{1}4\}$ surface. *Geochim. Cosmochim. Acta* **2010**, *74*, 2099−2109.

(124) Nehrke, G. *Calcite Precipitation from Aqueous Solution: Transformation from Vaterite and Role of Solution Stoichiometry*. Doctoral Dissertation, Utrecht University Department of Earth Sciences: The Netherlands, 2007. https://dspace.library.uu.nl/bitstream/handle/1874/19176/index.htm%3bsequence=11 (accessed 2021-04-22).

(125) Wolthers, M.; Nehrke, G.; Gustafsson, J. P.; Van Cappellen, P. Calcite growth kinetics: Modeling the effect of solution stoichiometry. *Geochim. Cosmochim. Acta* **2012**, *77*, 121−134.

(126) Garrels, R. M.; Christ, C. L. *Solutions, Minerals and Equilibria*; W. H. Freeman and Company: San Francisco, CA, USA, 1965.

(127) Morel, F. M. M.; Hering, J. G. *Principles and Applications of Aquatic Chemistry*; John Wiley & Sons: New York, NY, USA, 1993.

(128) Stumm, W.; Morgan, J. J. *Aquatic Chemistry: Chemical Equilibria and Rates in Natural Waters*; John Wiley & Sons, Inc.: NY, USA, 1996.

(129) Zhao, J.; Yang, D.; Yang, X. J.; Wu, B. Anion coordination chemistry: From recognition to supramolecular assembly. *Coord. Chem. Rev.* **2019**, *378*, 415−444.

(130) Zhang, J.; Nancollas, G. H. Kink density and rate of step movement during growth and dissolution of an *AB* Crystal in a Nonstoichiometric Solution. *J. Colloid Interface Sci.* **1998**, *200*, 131−145.

(131) Kowacz, M.; Prieto, M.; Putnis, A. Kinetics of crystal nucleation in ionic solutions: Electrostatics and hydration forces. *Geochim. Cosmochim. Acta* **2010**, *74*, 469−481.

(132) Voigt, A.; Sundmacher, K. Monte Carlo simulation of shape evolution in solutions − A model study of $BaSO_4$ precipitation. *Comput.-Aided Chem. Eng.* **2012**, *30*, 1163−1166.

(133) Vekilov, P. G. The two-step mechanism of nucleation of crystals in solution. *Nanoscale* **2010**, *2*, 2346−2357.

(134) Gurpinar, G.; Sonmez, E.; Bozkurt, V. Effect of ultrasonic treatment on flotation of calcite, barite and quartz. *Miner. Process. Extr. Metall.* **2004**, *113*, 91−95.

(135) Kecir, M.; Kecir, A. Efficiency of Barite Flotation Reagents - a Comparative Study. *J. Pol. Miner. Eng. Soc.* **2016**, *17*, 269−278.

(136) Ren, Z.; Yu, F.; Gao, H.; Chen, Z.; Peng, Y.; Liu, L. Selective separation of fluorite, barite and calcite with valonea extract and sodium fluosilicate as depressants. *Minerals* **2017**, *7*, 24.